

# Plasma etching of high aspect ratio features in SiO<sub>2</sub> using Ar/C<sub>4</sub>F<sub>8</sub>/O<sub>2</sub> mixtures: A computational investigation

Shuo Huang,<sup>1,a)</sup> Chad Huard,<sup>1,b)</sup> Seungbo Shim,<sup>2,c)</sup> Sang Ki Nam,<sup>2,d)</sup> In-Cheol Song,<sup>2,e)</sup> Siqing Lu,<sup>2,f)</sup> and Mark J. Kushner<sup>1,g)</sup>

<sup>1</sup>Department of Electrical Engineering and Computer Science, University of Michigan, 1301 Beal Ave., Ann Arbor, Michigan 48109-2122

<sup>2</sup>Samsung Electronics Co., Ltd., 129 Samsung-ro, Yeongtong-gu, Suwon-si, Gyeonggi-do 443-742, Republic of Korea

(Received 29 January 2019; accepted 18 March 2019; published 17 April 2019)

Plasma etching of high aspect ratio (HAR) features, typically vias, is a critical step in the fabrication of high capacity memory. With aspect ratios (ARs) exceeding 50 (and approaching 100), maintaining critical dimensions (CDs) while eliminating or diminishing twisting, contact-edge-roughening, and aspect ratio dependent etching (ARDE) becomes challenging. Integrated reactor and feature scale modeling was used to investigate the etching of HAR features in SiO<sub>2</sub> with ARs up to 80 using tri-frequency capacitively coupled plasmas sustained in Ar/C<sub>4</sub>F<sub>8</sub>/O<sub>2</sub> mixtures. In these systems, the fluxes of neutral radicals to the wafer exceed the fluxes of ions by 1–2 orders of magnitude due to lower threshold energies for dissociation compared with ionization. At low ARs (<5), these abundant fluxes of CF<sub>x</sub> and C<sub>x</sub>F<sub>y</sub> radicals to the etch front passivate the oxide to form a complex which is then removed by energetic species (ions and hot neutrals) through chemically enhanced reactive etching, resulting in the formation of gas phase SiF<sub>x</sub>, CO<sub>x</sub>, and COF. As the etching proceeds into higher ARs, the fractional contribution of physical sputtering to oxide removal increases as the fluxes of energetic species to the etch front surpass those of the conduction constrained CF<sub>x</sub> and C<sub>x</sub>F<sub>y</sub> radicals. The instantaneous etch rate of oxide decreases with increasing aspect ratio (ARDE effect) due to decreased fluxes of energetic species and decreased power delivered by these species to the etch front. As the etch rate of photoresist (PR) is independent of AR, maintaining CDs by avoiding undercut and bowing requires high SiO<sub>2</sub>-over-PR selectivity, which in turn requires a minimum thickness of the PR at the end of etching. Positive ions with narrow angular distributions typically deposit charge on the bottom of low AR features, producing a maximum in positive electric potential on the bottom of the feature. For high AR features, grazing incidence collisions of ions on sidewalls depositing charge produce electric potentials with maxima on the sidewalls (as opposed to the bottom) of the feature. *Published by the AVS.* <https://doi.org/10.1116/1.5090606>

## I. INTRODUCTION

Plasma etching of high aspect ratio (HAR) features in SiO<sub>2</sub> and Si<sub>3</sub>N<sub>4</sub> with aspect ratios (ARs) exceeding 100 is being challenged to maintain critical dimensions (CDs) and achieve high selectivity while etching stacks of materials for high capacity three-dimensional memory.<sup>1–3</sup> Controlling and mitigating phenomena such as aspect ratio dependent etching (ARDE), bowing, and contact edge roughness (CER) are necessary to obtain anisotropic features and better critical dimension uniformity (CDU). ARDE refers to a decrease in the etch rate for features having larger ARs for otherwise identical conditions. ARDE can occur for simultaneously etched features whose initial CDs (e.g., mask opening) have different sizes or within a single feature as the AR increases during etching. ARDE is a result of transport phenomena

that depend on AR and can be minimized through controlling the mass transfer rate to the etch front by tuning the bias power, gas pressure, or substrate temperature.<sup>4,5</sup> Bowing refers to the deviation of features from a purely anisotropic profile with straight walls to one having outward curvature. Bowing primarily results from the change in the acceptance angle of incident ions into the feature due to erosion of mask material and subsequent reflection from the facets of resist, diffusive particle scattering within the feature or scattering from rough surfaces.<sup>2,6</sup>

Maintaining CDU requires minimizing pattern distortion, in which an initially circular mask opening is not preserved through the depth of the feature, evolving into ellipses or other noncircular shapes.<sup>7–9</sup> CER originates from nonuniformities in the mask due to stochastic processes during etching or from the lithography-development process. These nonuniformities are then imprinted into the sidewalls of the feature by anisotropic delivery of activation energy.<sup>9,10</sup> Maintaining CDU also requires minimizing twisting, where the etch does not proceed strictly normal to the surface but deviates from the normal, and avoiding feature-to-feature variations in the total etch depth.<sup>6,11</sup> Many of these problems associated with CDU can be attributed to the stochastic nature of fluxes of radicals and ions incident into adjacent features. With the

<sup>a)</sup>Electronic mail: shuoh@umich.edu

<sup>b)</sup>Present address: KLA-Tencor Corp., 8834 N. Capital of Texas HW, Suite 301, Austin, TX 78759; electronic mail: chad.huard@kla.com

<sup>c)</sup>Electronic mail: seungb.shim@samsung.com

<sup>d)</sup>Electronic mail: sangki.j.nam@samsung.com

<sup>e)</sup>Electronic mail: ic13.song@samsung.com

<sup>f)</sup>Electronic mail: siqing.lu@samsung.com

<sup>g)</sup>Author to whom correspondence should be addressed: mjkuhs@umich.edu

CDs of features now less than 10 nm and the mask opening having a commensurately smaller area, the number and variety of particles incident into adjacent features is subject to statistical noise. The result is that adjacent features may receive different fluxes and sequencing of individual species. These statistical sources of CDU are not the result of reactor scale nonuniformities and may be addressed by employing self-limiting processes, such as atomic layer etching,<sup>12</sup> or increasing the magnitude of fluxes in inverse proportion to the decrease in mask opening.

In addition to the challenges resulting from high aspect ratio and nanoscale feature size, the etching of HAR features in SiO<sub>2</sub> typically uses a complex reaction mechanism with multiple steps based on the use of fluorocarbon gas mixtures. For example, increasing bias power produces a higher SiO<sub>2</sub> etch rate in HAR vias due to higher ion energies delivered through sheath acceleration while deforming the vias by bowing and edge roughening.<sup>13,14</sup> Energy-controlled and mass-selected CF<sub>2</sub><sup>+</sup> and CF<sub>3</sub><sup>+</sup> ion beams were used with the goal of controlling the surface atomic composition and so controlling the removal rate of SiO<sub>2</sub>.<sup>15,16</sup> Increasing the ion beam energy from 100 to 400 eV increased the F/O ratio of the surface layers due to enhanced surface fluorination and produced a higher etch yield of SiO<sub>2</sub>. Extremely high ion energies (several keV) damage SiO<sub>2</sub> and the underlying Si according to both experiments and numerical simulations. These effects can be mitigated by carefully controlling the overlying polymer thickness through the gas flow rate and the over-etch time.<sup>17,18</sup>

While being an etchant and providing activation energy, ions are also typically neutralized when striking surfaces on the top and inside of the feature. In doing so, positive charge is deposited on the surfaces.<sup>19</sup> Electrons also deposit charge, though due to their nearly isotropic trajectories incident onto the surface compared with ions, electron charging dominantly occurs on the top and upper portion of the features. Positive ions striking sidewalls at grazing angles neutralize and specularly reflect and then proceed as hot neutrals, retaining a large fraction of their initial energy. The electrical potential and electric fields produced by charge deposited on sidewalls and the etch front can deviate the trajectories of subsequent ions while reducing their energy, resulting in twisting and an etch stop. Pulsed power excitation can address many of the detriments of charging by elevating the ion energy,<sup>20</sup> reducing the thickness of fluorocarbon films on sidewalls,<sup>21</sup> and enabling the injection of negative ions to neutralize positive charge inside the feature.<sup>22,23</sup>

Optimizing plasma etching of HAR features requires precise control of both the fluxes of ions and neutrals. In fluorocarbon plasmas, fluxes of CF<sub>x</sub> neutrals are produced by electron impact dissociation followed by diffusion to the wafer. In the absence of charge exchange collisions in the sheath that may produce anisotropic neutral fluxes, these fluxes typically arrive at the substrate with isotropic trajectories. Increasing the C<sub>4</sub>F<sub>8</sub> flow rate or decreasing the O<sub>2</sub> flow rate in Ar/C<sub>4</sub>F<sub>8</sub>/O<sub>2</sub> mixtures increases SiO<sub>2</sub> etch rates due to the deposition of thicker fluorocarbon films produced by larger CF<sub>x</sub> fluxes to the surface.<sup>24</sup> Adding CH<sub>4</sub> or H<sub>2</sub> to C<sub>2</sub>F<sub>6</sub> gas mixtures results in decreased SiO<sub>2</sub> etch rates and

increased SiO<sub>2</sub>/Si selectivity by scavenging atomic fluorine in forming HF molecules, thereby decreasing the F/C flux ratio to the wafer.<sup>25</sup>

Etching of HAR features faces challenges in the delivery of thermal neutral radicals to the etch front whose incident velocities are isotropic and in the transport of etch products out of the feature. Due to the limits of vacuum conductance, the probability of neutral radicals entering into the feature reaching and reacting on the etch front at the bottom of the feature decreases with increasing AR.<sup>26</sup> This decreasing probability results from diffusive reflection from sidewalls during which some fraction of the incident flux is reflected back out of the feature to the plasma. The probability of reacting at the etch front further decreases if the radicals have a nonzero probability for reacting on sidewalls.<sup>26</sup> The same trends apply to thermal etch products produced at the bottom of the feature. The larger the AR, the larger the number of collisions etch products will have with the surface inside the feature prior to exiting the top of the feature. These large number of collisions may result in a redeposition of the etch products. Conductance limits result in decreased neutral etchant delivery from the top to the bottom of the feature and redeposition of etch products in transport from the bottom to the top of the feature, both of which can produce lower etch rates. These effects can be partially mitigated by regulating the sticking coefficient of radicals to the sidewall through controlling the wafer temperature.<sup>27–29</sup>

Conductance limitations of neutral transport into HAR features largely result from the radicals having initially isotropic trajectories and diffusive isotropic scattering from sidewalls. Hot neutrals produced through neutralization of energetic ions at surfaces have higher conductance to the etch front than the thermal neutrals due to their initially more anisotropic angular distributions and more specular scattering. These hot neutrals deliver both energy to the etch front and, upon slowing deeper in the feature, neutral reactivity which enables etching to proceed at high ARs. A molecular dynamics simulation was used to investigate the consequences of hot CF<sub>2</sub> and CF<sub>3</sub> radicals in SiO<sub>2</sub> etching.<sup>19,30</sup> At low energies (10 eV), CF<sub>2</sub> was the main etchant to break the Si–O bond due to its higher chemical reactivity. At high energies (150 eV), CF<sub>3</sub> became the main etchant due to the production of more reactive F atoms, resulting in the formation of more Si–F bonds. The etch yield was found to depend on the incident angle of hot radicals to the surface. An irradiation angle of 60° resulted in the maximum yield of Si and O from the SiO<sub>2</sub> surface.<sup>31</sup>

Computational models for SiO<sub>2</sub> etching have been developed to investigate feature profiles in the etching of gate dielectrics (AR < 10) and conduction channel holes through insulating layers (AR > 50). An integrated reactor and feature scale model was used to investigate the etching of topographic layered and self-aligned Si<sub>3</sub>N<sub>4</sub>/SiO<sub>2</sub> structures using fluorocarbon plasmas.<sup>32</sup> The Si<sub>3</sub>N<sub>4</sub>/SiO<sub>2</sub> selectivity was optimized by controlling the thickness of the polymer at the top of the feature by tuning the time during etching and deposition phases in a cyclic plasma etch process. A semiempirical profile simulator was employed to investigate the necking and bowing of etching of HAR features.<sup>33</sup> The necking resulted from a balance between polymer removal and deposition

processes, while the bowing was caused by surface scattering of ions from secondary facets. Nonuniform necking was found to cause an imbalance in the ion flux to the bottom of the feature, resulting in twisting irrespective of charging.<sup>6</sup>

Results from a voxel-slab model, developed to investigate contact hole etching in SiO<sub>2</sub>, indicated that physical damage was reduced by maintaining a critical thickness of the overlying polymer.<sup>17,34</sup> Bowing during the etching of HAR features was found to result from excessive fluxes of F and O radicals to the sidewalls according to the results of a line-of-sight profile simulator.<sup>35</sup> A model addressing pattern deformation and experimental measurements by atomic force microscopy indicated that the ratio of line width roughness to line edge roughness decreases with increasing etch depth, and the depth at which twisting occurs is shallower for a lower bias power.<sup>1</sup>

In this paper, results are discussed from integrated reactor and feature scale models for investigating the etching of HAR features in SiO<sub>2</sub> using a tri-frequency capacitively coupled plasma (TF-CCP) sustained in Ar/C<sub>4</sub>F<sub>8</sub>/O<sub>2</sub> mixtures at several tens of mTorr. Reactor scale modeling was performed using the two-dimensional hybrid plasma equipment model (HPEM), from which the fluxes, energy, and angular distributions of ions and neutrals to the wafer surface were obtained. The feature scale modeling was performed using the three-dimensional Monte Carlo feature profile model (MCFPM). We found that at low ARs where neutral transport is not conductance limited, abundant fluxes of CF<sub>x</sub> and C<sub>x</sub>F<sub>y</sub> radicals to the etch front passivate the oxide to form a complex. This complex is then removed by ions and hot neutrals through chemically enhanced reactive etching (i.e., chemical sputtering) with the formation of gas phase SiF<sub>x</sub>, CO<sub>x</sub>, and COF etch products. As the etching proceeds to higher ARs, the fractional contribution of physical sputtering increases, as the fluxes of ions and hot neutrals to the etch front surpass those of the conduction constrained CF<sub>x</sub> and C<sub>x</sub>F<sub>y</sub> radicals. The general trend of ARDE, decreased instantaneous etch rate with increasing AR, mainly occurs due to decreased power delivery to the etch front while the flux of conduction limited neutrals also decreases.

The models used in this paper are described in Sec. II. The surface reaction mechanism for the etching of SiO<sub>2</sub> by Ar/C<sub>4</sub>F<sub>8</sub>/O<sub>2</sub> mixtures used in MCFPM is described in Sec. III. Results from the reactor scale modeling of TF-CCP sustained in Ar/C<sub>4</sub>F<sub>8</sub>/O<sub>2</sub> mixtures are discussed in Sec. IV. Results from feature scale modeling of HAR etching of SiO<sub>2</sub> are discussed in Sec. V. Concluding remarks are given in Sec. VI.

## II. DESCRIPTION OF THE MODELS

Reactor scale modeling of the TF-CCP sustained in Ar/C<sub>4</sub>F<sub>8</sub>/O<sub>2</sub> mixtures was performed with the two-dimensional HPEM.<sup>36</sup> The HPEM combines fluid and kinetic methods, using a hierarchical approach where modules addressing different physical processes exchange information on different time scales. The major modules used in this study are the fluid kinetics Poisson module (FKPM), the Electron Energy

Transport Module (EETM), and the plasma chemistry Monte Carlo module (PCMCM).

The densities, fluxes, and temperatures of charged and neutral species and electrostatic potentials are obtained from the FKPM. Continuity, momentum, and energy equations for all species are solved coincident with Poisson's equation for the electrostatic potential. Charge densities on the surfaces of the dielectrics are computed from the incident fluxes of electrons and ions from the bulk plasma, fluxes of secondary electrons leaving the surfaces and coming from other locations collected by those surfaces, and conduction currents through the material. The electron energy equation is implicitly integrated in time to provide the electron temperature. Electron impact rate coefficients and transport coefficients are obtained from the EETM in which Boltzmann's equation is solved for the electron energy distribution. The trajectories of secondary electrons are advanced using Monte Carlo techniques in the EETM.

When the calculated plasma properties reach steady state, the PCMCM is executed to compute ion and neutral trajectories from the bulk plasma through the time-varying sheath with source functions for generation of the ions and electric fields from the FKPM.<sup>37</sup> Pseudoparticles that represent ions and neutrals are launched at locations weighted by their source functions throughout the plasma volume. The trajectories of the pseudoparticles are integrated by interpolating electric fields in time and space to compute accelerations. The energy and angular distributions of pseudoparticles striking the wafer surface are collected and averaged over the radio frequency (rf) cycle.

The time evolution of profiles etched in SiO<sub>2</sub> using fluxes, energy, and angular distributions of ions and neutrals provided by the HPEM are predicted by the MCFPM, described in detail in Ref. 38. Briefly, in the MCFPM, the feature is resolved using a three-dimensional cubic mesh. A material identity is assigned to each cell in the mesh, often called a voxel. Gas phase species are represented by Monte Carlo pseudoparticles which are launched with energies and angles sampled from the distributions obtained from the HPEM. The trajectories of the pseudoparticles are tracked until they hit a solid mesh cell, where a surface reaction mechanism is used to determine the disposition of the gas particle and solid cell using Monte Carlo techniques. Based on the selected reaction, the identity of the mesh cell at the site of collision will be changed (e.g., passivation), removed into the gas phase (e.g., etching), or covered by a new mesh cell (e.g., deposition).

In the MCFPM, the occurrence of each reaction is determined by the probabilities listed in the reaction mechanisms summarized in Table I. Probability arrays for the reaction of each gas phase species with each surface site are constructed while accounting for the energy and angular dependence of the process. When a pseudoparticle hits a surface cell, a random number is generated to select the reaction that would occur based on these probability arrays. For etching reactions having an energy dependence (e.g., physical sputtering and chemically enhanced etching), the reaction yield for a particle incident onto a surface with an incident energy of  $E_i$  and an incident angle of  $\theta$  with respect to the local surface

TABLE I. Surface reaction mechanism for plasma etching of SiO<sub>2</sub> in Ar/C<sub>4</sub>F<sub>8</sub>/O<sub>2</sub> mixtures.

Gas phase species					Notes
Ions, hot neutrals, and neutral partners	Ar <sup>+</sup> , Ar(h), Ar F <sup>+</sup> , F(h), F F <sub>2</sub> <sup>+</sup> , F <sub>2</sub> (h), F <sub>2</sub> O <sup>+</sup> , O(h), O O <sub>2</sub> <sup>+</sup> , O <sub>2</sub> (h), O <sub>2</sub> C <sub>m</sub> F <sub>n</sub> <sup>+</sup> , C <sub>m</sub> F <sub>n</sub> (h), C <sub>m</sub> F <sub>n</sub>				a
Etch products	CO, CO <sub>2</sub> , COF, COH SiF <sub>x</sub> , SiF <sub>4</sub>				b
Sputtered materials	R, SiO <sub>2</sub> , Si				c
Surface sites					Notes
Photoresist	R(s)				
Silicon oxide	SiO <sub>2</sub> (s)				
Passivated oxide surface (complex)	SiO <sub>2</sub> C <sub>m</sub> F <sub>n</sub> (s) SiOCF <sub>3</sub> (s)				d
Silicon	Si(s)				
Fluorinated silicon surface	SiF <sub>x</sub> (s)				e
Polymer	P(s)				
Activated surface sites	SiO <sub>2</sub> * (s) SiO <sub>2</sub> C <sub>m</sub> F <sub>n</sub> * (s) SiOCF <sub>3</sub> * (s) P* (s)				f
Reactions <sup>g</sup>	$p_0^h$	$E_{th}$ (eV) <sup>h</sup>	$E_r$ (eV) <sup>h</sup>	Notes	
<i>Activation of SiO<sub>2</sub></i>					
SiO <sub>2</sub> (s) + I <sup>+</sup> → SiO <sub>2</sub> * (s) + I(h)	0.9			i	
<i>Sputtering of SiO<sub>2</sub></i>					
SiO <sub>2</sub> (s) + I <sup>+</sup> → SiO <sub>2</sub> + I(h)	0.9	70	140	ij	
SiO <sub>2</sub> * (s) + I <sup>+</sup> → SiO <sub>2</sub> + I(h)	0.9	70	140	ij	
<i>Passivation of SiO<sub>2</sub></i>					
SiO <sub>2</sub> (s) + CF → SiO <sub>2</sub> CF(s)	0.4			Ref. 39	
SiO <sub>2</sub> (s) + CF <sub>2</sub> → SiO <sub>2</sub> CF <sub>2</sub> (s)	0.3			Ref. 39	
SiO <sub>2</sub> (s) + CF <sub>3</sub> → SiO <sub>2</sub> CF <sub>3</sub> (s)	0.2			Ref. 39	
SiO <sub>2</sub> (s) + C <sub>2</sub> F <sub>3</sub> → SiO <sub>2</sub> C <sub>2</sub> F <sub>3</sub> (s)	0.2			Ref. 39, <sup>k</sup>	
SiO <sub>2</sub> * (s) + CF <sub>x</sub> → SiO <sub>2</sub> CF <sub>x</sub> (s)	0.9			k,l	
SiO <sub>2</sub> * (s) + C <sub>2</sub> F <sub>3</sub> → SiO <sub>2</sub> C <sub>2</sub> F <sub>3</sub> (s)	0.9			k	
<i>Further passivation of complex</i>					
SiO <sub>2</sub> CF(s) + CF <sub>2</sub> → SiO <sub>2</sub> C <sub>2</sub> F <sub>3</sub> (s)	10 <sup>-4</sup>				
SiO <sub>2</sub> CF <sub>2</sub> (s) + CF → SiO <sub>2</sub> C <sub>2</sub> F <sub>3</sub> (s)	10 <sup>-4</sup>				
SiO <sub>2</sub> CF <sub>2</sub> (s) + CF <sub>2</sub> → SiO <sub>2</sub> C <sub>2</sub> F <sub>4</sub> (s)	10 <sup>-4</sup>				
SiO <sub>2</sub> CF <sub>2</sub> (s) + C <sub>2</sub> F <sub>3</sub> → SiO <sub>2</sub> C <sub>3</sub> F <sub>5</sub> (s)	10 <sup>-4</sup>				
SiO <sub>2</sub> CF <sub>3</sub> (s) + CF → SiO <sub>2</sub> C <sub>2</sub> F <sub>4</sub> (s)	10 <sup>-4</sup>				
SiO <sub>2</sub> CF <sub>3</sub> (s) + C <sub>2</sub> F <sub>3</sub> → SiO <sub>2</sub> C <sub>3</sub> F <sub>6</sub> (s)	10 <sup>-4</sup>				
SiO <sub>2</sub> C <sub>2</sub> F <sub>3</sub> (s) + CF <sub>2</sub> → SiO <sub>2</sub> C <sub>3</sub> F <sub>5</sub> (s)	10 <sup>-4</sup>				
SiO <sub>2</sub> C <sub>2</sub> F <sub>4</sub> (s) + CF → SiO <sub>2</sub> C <sub>3</sub> F <sub>5</sub> (s)	10 <sup>-4</sup>				
SiO <sub>2</sub> C <sub>2</sub> F <sub>4</sub> (s) + CF <sub>2</sub> → SiO <sub>2</sub> C <sub>3</sub> F <sub>6</sub> (s)	10 <sup>-4</sup>				
<i>Fluorination of passivated surface</i>					
SiO <sub>2</sub> CF(s) + F → SiO <sub>2</sub> CF <sub>2</sub> (s)	0.1				
SiO <sub>2</sub> CF <sub>2</sub> (s) + F → SiO <sub>2</sub> CF <sub>3</sub> (s)	0.1				
SiO <sub>2</sub> C <sub>2</sub> F <sub>3</sub> (s) + F → SiO <sub>2</sub> C <sub>2</sub> F <sub>4</sub> (s)	0.1				
SiO <sub>2</sub> C <sub>3</sub> F <sub>5</sub> (s) + F → SiO <sub>2</sub> C <sub>3</sub> F <sub>6</sub> (s)	0.1				
<i>Etching of passivated surface complex</i>					
SiO <sub>2</sub> CF(s) + I <sup>+</sup> → SiF + CO <sub>2</sub> + I(h)	0.75	35	140	i,m	
SiO <sub>2</sub> CF <sub>2</sub> (s) + I <sup>+</sup> → SiF <sub>2</sub> + CO <sub>2</sub> + I(h)	0.75	35	140	i,m	
SiO <sub>2</sub> CF <sub>3</sub> (s) + I <sup>+</sup> → SiF <sub>3</sub> + CO <sub>2</sub> + I(h)	0.75	35	140	i,m	
SiO <sub>2</sub> C <sub>2</sub> F <sub>3</sub> (s) + I <sup>+</sup> → SiOCF <sub>3</sub> (s) + CO + I(h)	0.75	35	140	i,m	
SiO <sub>2</sub> C <sub>2</sub> F <sub>4</sub> (s) + I <sup>+</sup> → SiOCF <sub>3</sub> (s) + COF + I(h)	0.75	35	140	i,m	
SiO <sub>2</sub> C <sub>3</sub> F <sub>5</sub> (s) + I <sup>+</sup> → SiO <sub>2</sub> CF(s) + C <sub>2</sub> F <sub>4</sub> + I(h)	0.75	35	140	i,m	

TABLE I. Continued

Reactions <sup>g</sup>	$p_0^h$	$E_{th}$ (eV) <sup>h</sup>	$E_r$ (eV) <sup>h</sup>	Notes
SiO <sub>2</sub> C <sub>3</sub> F <sub>6</sub> (s) + I <sup>+</sup> → SiO <sub>2</sub> CF <sub>3</sub> (s) + C <sub>2</sub> F <sub>3</sub> + I(h)	0.75	35	140	i,m
SiOCF <sub>3</sub> (s) + I <sup>+</sup> → SiF <sub>3</sub> + CO + I(h)	0.75	35	140	i,m
SiO <sub>2</sub> CF <sub>2</sub> *(s) + I <sup>+</sup> → SiF + CO <sub>2</sub> + I(h)	0.75	35	140	i,m
SiO <sub>2</sub> CF <sub>2</sub> * <sup>*</sup> (s) + I <sup>+</sup> → SiF <sub>2</sub> + CO <sub>2</sub> + I(h)	0.75	35	140	i,m
SiO <sub>2</sub> CF <sub>3</sub> * <sup>*</sup> (s) + I <sup>+</sup> → SiF <sub>3</sub> + CO <sub>2</sub> + I(h)	0.75	35	140	i,m
SiO <sub>2</sub> C <sub>2</sub> F <sub>3</sub> * <sup>*</sup> (s) + I <sup>+</sup> → SiOCF <sub>3</sub> (s) + CO + I(h)	0.75	35	140	i,m
SiO <sub>2</sub> C <sub>2</sub> F <sub>4</sub> * <sup>*</sup> (s) + I <sup>+</sup> → SiOCF <sub>3</sub> (s) + COF + I(h)	0.75	35	140	i,m
SiO <sub>2</sub> C <sub>3</sub> F <sub>5</sub> * <sup>*</sup> (s) + I <sup>+</sup> → SiO <sub>2</sub> CF(s) + C <sub>2</sub> F <sub>4</sub> + I(h)	0.75	35	140	i,m
SiO <sub>2</sub> C <sub>3</sub> F <sub>6</sub> * <sup>*</sup> (s) + I <sup>+</sup> → SiO <sub>2</sub> CF <sub>3</sub> (s) + C <sub>2</sub> F <sub>3</sub> + I(h)	0.75	35	140	i,m
SiOCF <sub>3</sub> * <sup>*</sup> (s) + I <sup>+</sup> → SiF <sub>3</sub> + CO + I(h)	0.75	35	140	i,m
<i>Polymer deposition on activated complex</i>				
SiO <sub>2</sub> C <sub>m</sub> F <sub>n</sub> * <sup>*</sup> (s) + CF → SiO <sub>2</sub> C <sub>m</sub> F <sub>n</sub> * <sup>*</sup> (s) + P(s)	0.002			
SiO <sub>2</sub> C <sub>m</sub> F <sub>n</sub> * <sup>*</sup> (s) + CF <sub>2</sub> → SiO <sub>2</sub> C <sub>m</sub> F <sub>n</sub> * <sup>*</sup> (s) + P(s)	0.0015			
SiO <sub>2</sub> C <sub>m</sub> F <sub>n</sub> * <sup>*</sup> (s) + CF <sub>3</sub> → SiO <sub>2</sub> C <sub>m</sub> F <sub>n</sub> * <sup>*</sup> (s) + P(s)	0.001			
SiO <sub>2</sub> C <sub>m</sub> F <sub>n</sub> * <sup>*</sup> (s) + C <sub>x</sub> F <sub>y</sub> → SiO <sub>2</sub> C <sub>m</sub> F <sub>n</sub> * <sup>*</sup> (s) + P(s)	0.001			k
SiOCF <sub>3</sub> * <sup>*</sup> (s) + CF → SiOCF <sub>3</sub> * <sup>*</sup> (s) + P(s)	0.002			
SiOCF <sub>3</sub> * <sup>*</sup> (s) + CF <sub>2</sub> → SiOCF <sub>3</sub> * <sup>*</sup> (s) + P(s)	0.0015			
SiOCF <sub>3</sub> * <sup>*</sup> (s) + CF <sub>3</sub> → SiOCF <sub>3</sub> * <sup>*</sup> (s) + P(s)	0.001			
SiOCF <sub>3</sub> * <sup>*</sup> (s) + C <sub>x</sub> F <sub>y</sub> → SiOCF <sub>3</sub> * <sup>*</sup> (s) + P(s)	0.001			k
<i>Polymer deposition on polymer</i>				
P(s) + CF → P(s) + P(s)	0.002			
P(s) + CF <sub>2</sub> → P(s) + P(s)	0.0015			
P(s) + CF <sub>3</sub> → P(s) + P(s)	0.001			
P(s) + C <sub>x</sub> F <sub>y</sub> → P(s) + P(s)	0.001			k
P*(s) + CF → P*(s) + P(s)	0.02			
P*(s) + CF <sub>2</sub> → P*(s) + P(s)	0.015			
P*(s) + CF <sub>3</sub> → P*(s) + P(s)	0.01			
P*(s) + C <sub>x</sub> F <sub>y</sub> → P*(s) + P(s)	0.01			k
<i>Polymer chemical sputtering</i>				
P(s) + I <sup>+</sup> → I(h) + CF <sub>2</sub>	0.3	30	140	j,n
P*(s) + I <sup>+</sup> → I(h) + CF <sub>2</sub>	0.3	30	140	j,n
P(s) + O <sup>+</sup> → COF	0.2	20	100	m
P(s) + O <sub>2</sub> <sup>+</sup> → O(h) + COF	0.2	20	100	m
P*(s) + O <sup>+</sup> → COF	0.2	20	100	m
P*(s) + O <sub>2</sub> <sup>+</sup> → O(h) + COF	0.2	20	100	m
<i>Polymer chemical erosion</i>				
P(s) + F → CF <sub>2</sub>	0.001			
P*(s) + F → CF <sub>2</sub>	0.03			
P(s) + O → COF	0.5			
P*(s) + O → COF	0.9			
<i>Fluorination and etching of Si</i>				
Si(s) + F → SiF(s)	0.01			
SiF(s) + F → SiF <sub>2</sub> (s)	0.02			
SiF <sub>2</sub> (s) + F → SiF <sub>3</sub> (s)	0.03			
SiF <sub>3</sub> (s) + F → SiF <sub>4</sub>	0.05			
<i>Chemical, physical sputtering Si(s), SiF<sub>x</sub>(s)</i>				
Si(s) + I <sup>+</sup> → Si + I(h)	0.1	37.5	100	Ref. 40, <sup>ij</sup>
SiF(s) + I <sup>+</sup> → SiF + I(h)	0.3	10	100	i,m
SiF <sub>2</sub> (s) + I <sup>+</sup> → SiF <sub>2</sub> + I(h)	0.4	10	100	i,m
SiF <sub>3</sub> (s) + I <sup>+</sup> → SiF <sub>3</sub> + I(h)	0.5	10	100	i,m
<i>Polymer deposition on Si(s) and SiF<sub>x</sub>(s)</i>				
Si(s) + CF → Si(s) + P(s)	0.5			
Si(s) + CF <sub>2</sub> → Si(s) + P(s)	0.375			
Si(s) + CF <sub>3</sub> → Si(s) + P(s)	0.25			
Si(s) + C <sub>x</sub> F <sub>y</sub> → Si(s) + P(s)	0.25			k
SiF <sub>x</sub> (s) + CF → SiF <sub>x</sub> (s) + P(s)	0.002			
SiF <sub>x</sub> (s) + CF <sub>2</sub> → SiF <sub>x</sub> (s) + P(s)	0.0015			
SiF <sub>x</sub> (s) + CF <sub>3</sub> → SiF <sub>x</sub> (s) + P(s)	0.001			
SiF <sub>x</sub> (s) + C <sub>x</sub> F <sub>y</sub> → SiF <sub>x</sub> (s) + P(s)	0.001			k

TABLE I. Continued

Reactions <sup>g</sup>	$p_0^h$	$E_{th}$ (eV) <sup>h</sup>	$E_r$ (eV) <sup>h</sup>	Notes
<i>Redeposition of SiF<sub>x</sub></i>				
P(s) + SiF <sub>x</sub> → P(s) + SiF <sub>x</sub> (s)	0.001			
<i>Erosion of photoresist</i>				
R(s) + I <sup>+</sup> → R + I(h)	0.01	20	100	ij
R(s) + O → COH	10 <sup>-5</sup>			
<i>Redeposition of gas phase photoresist</i>				
W(s) + R → W(s) + R(s)	0.01			o
<i>Polymer deposition on photoresist</i>				
R(s) + CF → R(s) + P(s)	0.02			
R(s) + CF <sub>2</sub> → R(s) + P(s)	0.015			
R(s) + CF <sub>3</sub> → R(s) + P(s)	0.01			
R(s) + C <sub>x</sub> F <sub>y</sub> → R(s) + P(s)	0.01			k
	$p_0^p$	$E_{th}$ (eV) <sup>p</sup>	$E_m$ (eV) <sup>p</sup>	Notes
<i>Activation by low energy ions</i>				
SiO <sub>2</sub> C <sub>m</sub> F <sub>n</sub> (s) + I <sup>+</sup> → SiO <sub>2</sub> C <sub>m</sub> F <sub>n</sub> <sup>*</sup> (s) + I(h)	0.1	5	70	ij
SiOCF <sub>3</sub> (s) + I <sup>+</sup> → SiOCF <sub>3</sub> <sup>*</sup> (s) + I(h)	0.1	5	70	ij
P(s) + M <sup>+</sup> → P <sup>*</sup> (s) + M(h)	0.3	5	30	ij,q
<i>Polymer deposition by low energy ions</i>				
SiO <sub>2</sub> C <sub>m</sub> F <sub>n</sub> (s) + CF <sub>x</sub> <sup>+</sup> → SiO <sub>2</sub> C <sub>m</sub> F <sub>n</sub> (s) + P(s)	0.1	5	70	j,k
SiO <sub>2</sub> C <sub>m</sub> F <sub>n</sub> (s) + C <sub>x</sub> F <sub>y</sub> <sup>+</sup> → SiO <sub>2</sub> C <sub>m</sub> F <sub>n</sub> (s) + P(s)	0.1	5	70	j,k
SiOCF <sub>3</sub> (s) + CF <sub>x</sub> <sup>+</sup> → SiOCF <sub>3</sub> (s) + P(s)	0.1	5	70	j,k
SiOCF <sub>3</sub> (s) + C <sub>x</sub> F <sub>y</sub> <sup>+</sup> → SiOCF <sub>3</sub> (s) + P(s)	0.1	5	70	j,k

<sup>a</sup>C<sub>m</sub>F<sub>n</sub><sup>+</sup> denotes CF<sup>+</sup>, CF<sub>2</sub><sup>+</sup>, CF<sub>3</sub><sup>+</sup>, C<sub>2</sub>F<sub>3</sub><sup>+</sup>, C<sub>2</sub>F<sub>4</sub><sup>+</sup>, C<sub>2</sub>F<sub>5</sub><sup>+</sup>, C<sub>3</sub>F<sub>5</sub><sup>+</sup>, C<sub>3</sub>F<sub>6</sub><sup>+</sup>, C<sub>3</sub>F<sub>7</sub><sup>+</sup>, C<sub>4</sub>F<sub>7</sub><sup>+</sup>, and C<sub>4</sub>F<sub>8</sub><sup>+</sup>. C<sub>m</sub>F<sub>n</sub>(h) and C<sub>m</sub>F<sub>n</sub> are hot neutrals and thermal neutral partners of C<sub>m</sub>F<sub>n</sub><sup>+</sup> species.

<sup>b</sup>SiF<sub>x</sub> denotes SiF, SiF<sub>2</sub>, and SiF<sub>3</sub>.

<sup>c</sup>R is the sputtered photoresist in the gas phase.

<sup>d</sup>SiO<sub>2</sub>C<sub>m</sub>F<sub>n</sub>(s) represents SiO<sub>2</sub>CF(s), SiO<sub>2</sub>CF<sub>2</sub>(s), SiO<sub>2</sub>CF<sub>3</sub>(s), SiO<sub>2</sub>C<sub>2</sub>F<sub>3</sub>(s), SiO<sub>2</sub>C<sub>2</sub>F<sub>4</sub>(s), SiO<sub>2</sub>C<sub>3</sub>F<sub>5</sub>(s), and SiO<sub>2</sub>C<sub>3</sub>F<sub>6</sub>(s).

<sup>e</sup>SiF<sub>x</sub>(s) denotes SiF(s), SiF<sub>2</sub>(s), and SiF<sub>3</sub>(s).

<sup>f</sup>SiO<sub>2</sub>C<sub>m</sub>F<sub>n</sub><sup>\*</sup>(s) and P<sup>\*</sup>(s) represent activated surface partners of SiO<sub>2</sub>C<sub>m</sub>F<sub>n</sub>(s) and P(s).

<sup>g</sup>All ions neutralize on surfaces, returning to gas phase as their hot neutral partner. Ions and their hot neutral partners have the same surface reactions with the same probability. Only surface reactions for ions are shown in the table. All such reactions (with the exception of neutralization) should be duplicated for the ion's hot neutral partner.

<sup>h</sup>If  $E_{th}$  and  $E_r$  are blank, the reaction has no energy dependence and the probability of the reaction is a constant,  $p_0$ . If  $E_{th}$  and  $E_r$  have nonzero values, the reaction has an energy dependent probability [Eq. (1)]. When the probability of reaction is less than unity, the remaining probability is allocated to nonreactive reflection.

<sup>i</sup>I<sup>+</sup> denotes all positive ions. I(h) is the hot neutral partner produced by neutralization of I<sup>+</sup> at a surface.

<sup>j</sup>Reaction with physical sputtering angular dependence.

<sup>k</sup>CF<sub>x</sub> denotes CF, CF<sub>2</sub>, and CF<sub>3</sub>, CF<sub>x</sub><sup>+</sup> and CF<sub>x</sub>(h) denote the ion and hot neutral partners of CF<sub>x</sub>, respectively. Multicarbon fluorocarbon radicals having two or more dangling bonds are included in the reaction mechanism, collectively referred to as C<sub>x</sub>F<sub>y</sub>. For the purpose of describing specific reactions, C<sub>2</sub>F<sub>3</sub> is used as an example. C<sub>x</sub>F<sub>y</sub><sup>+</sup> and C<sub>x</sub>F<sub>y</sub>(h) denote the ion and hot neutral partners of C<sub>x</sub>F<sub>y</sub>, respectively.

<sup>l</sup>SiO<sub>2</sub>CF<sub>x</sub>(s) denotes the group of passivated oxide surface sites by CF<sub>x</sub> species, which are SiO<sub>2</sub>CF(s), SiO<sub>2</sub>CF<sub>2</sub>(s), and SiO<sub>2</sub>CF<sub>3</sub>(s).

<sup>m</sup>Reaction with chemical sputtering angular dependence.

<sup>n</sup>Polymer sputtered by hot neutrals and ions into the gas phase is represented by CF<sub>2</sub>.

<sup>o</sup>W(s) represents all surface sites.

<sup>p</sup>Probability of surface activation and polymer deposition by low energy ions [Eq. (2)].

<sup>q</sup>M<sup>+</sup> represents all ions except O<sup>+</sup> and O<sub>2</sub><sup>+</sup>. M(h) denotes the hot neutral partner of M<sup>+</sup>.

normal is determined by<sup>41,42</sup>

$$p(E_i, \theta) = p_0 \left( \frac{E_i - E_{th}}{E_r - E_{th}} \right)^n f(\theta), \quad (1)$$

where  $E_{th}$  is the threshold energy,  $E_r$  is the reference energy,  $p_0$  is the yield at the reference energy,  $n$  is the energy dependent exponent (typically 0.5), and  $f(\theta)$  is the relative probability at angle of incidence  $\theta$ .

The angular dependence is often different between direct physical sputtering and chemically enhanced etching. These

two processes can be simultaneously active, with chemically enhanced etching dominating at low ion energy and physical sputtering becoming more important as ion energy increases.<sup>43,44</sup> For physical sputtering,  $f(\theta)$  is an empirical function with a maximum at 60°, with reduced probability at normal incidence and zero probability at grazing incidence.<sup>42</sup> For chemically enhanced etching,  $f(\theta)$  is unity for normal incidence and angles up to 45°, with a monotonic roll-off to zero probability at grazing incidence.

Other than being etched by high energy ions with a reaction yield determined by Eq. (1), the surface complex and

polymers can be activated when the energy of the bombarding ions is low. These activated sites model the formation of dangling bonds on the surface due to low energy ion bombardment. The activated site, with its larger number of available dangling bonds, then has a higher sticking probability for CF<sub>x</sub> radicals for polymer deposition. The probability of activation of the complex and polymer sites by low energy ions is

$$p(E_i, \theta) = p_0 \times \max\left(0, 1 - \frac{E_i}{E_m}\right) f(\theta), \quad (2)$$

where  $E_m$  is the maximum energy of the process and  $p_0$  is the yield at zero incident energy.

Since the probability of a particle striking the surface upon arrival is, by definition, unity, the following procedure is followed to normalize the selection of reaction probabilities. The cumulative yield of all allowed processes for the energy and angle of incidence is computed. For all such interactions, there is an elastic collision, meaning a reflection from the surface without changing the state of the surface. If the cumulative yield of nonreflective processes is less than unity, then the elastic scattering yield is increased so that the cumulative yield is unity. If the cumulative yield is greater than unity, the elastic yield is reduced so that the cumulative yield is unity. If after scaling the elastic yield to zero, the cumulative yield is still greater than unity, then the yields of all processes are scaled to provide a unity cumulative yield. The scaled probability array is then used to randomly select the process that occurs.

In the etching of HAR features, energetic particles (originating as ions and proceeding as hot neutrals) can undergo several collisions with the sidewalls before reaching the etch front. In the MCFPM, an angle dependent energy loss is used to determine the retained energy of the reflected particle after colliding with the surface. For an energetic particle striking a surface with an incident energy of  $E_i$  and an incident angle of  $\theta$ , the energy of the scattered particle is determined by

$$E_s(\theta) = E_i \left( \frac{E_i - E_c}{E_{ts} - E_c} \right) \left( \frac{\theta - \theta_c}{90^\circ - \theta_c} \right) \quad \theta > \theta_c \quad \text{and} \quad (3)$$

$$E_c < E_i < E_{ts},$$

where  $E_{ts}$  is the threshold for complete specular scattering, which is 100 eV in this study.  $E_c$  is the cutoff energy for diffusive scattering, which is 10 eV for these simulations.  $\theta_c$  is the lower cutoff angle for specular reflection, which is 70° here. Incident particles with  $E_i > E_{ts}$  are assumed to retain all of their energy. Incident particles with  $\theta < \theta_c$  or  $E_i < E_c$  are assumed to diffusively scatter.

All positive ions neutralize upon their first collision with a surface, with the former ion proceeding as a hot neutral with an angle and energy given by the previous expressions. Other than for the neutralizing collision with the surface, hot neutrals have the same reaction mechanism as that of ions. When the energy of a hot neutral falls below 5 eV, it is reclassified as a thermal neutral.

Electrostatic charging of features results from the deposition of charge from ions which neutralize upon striking

surfaces (top of feature or sidewalls within features) and electrons. Charge is then retained on the voxel upon which it is deposited until neutralized by electrons (for positive charge) or ions (for negative charge). If a voxel with charge is removed through surface reactions (e.g., physical and chemical sputtering), the removed cell does not carry away its charge into the gas phase. The charge is retained in the mesh by redistributing the charge to the adjacent mesh cells. The voxel harboring the charge can also be buried by polymer or redeposition of etch products. This surface-resident or buried charge produces electric fields which in turn accelerate or deviate the trajectories of incident charged particles. The changes in velocities of charged particles from these electric fields are included in the simulation by adding the resulting Lorentz forces to the equations of motion of charged particles as their trajectories are integrated. These electric fields are computed in the following manner.

On a time averaged basis, the net conduction current to the wafer in a capacitively coupled plasma is zero. With this boundary condition, the net flux of positive and negative ions launched toward the feature is balanced by a flux of electrons to sum to zero net current. The initial trajectories and fluxes of ions are given by the PCMCM. The current of ions launched toward the surface is determined from the randomly chosen fluxes. A corresponding flux of electron pseudoparticles is also launched to provide charge neutrality. In CCPs, the electron flux typically arrives at the surface only when the sheath collapses during the anodic portion of the cycle. The trajectories of the electrons therefore arrive at the surface with nearly isotropic trajectories having a temperature nearly the same as in the bulk plasma. Electron pseudoparticles are therefore launched toward the feature with velocity randomly chosen from an isotropic Maxwellian distribution having a specified temperature. Although experimentally electrons typically arrive at the surface in bursts during the anodic portion of the cycle, in the simulation, an electron particle is launched after every positive ion particle is launched with adjustments made if negative ions are also launched.

The algorithms for computing electric fields in the feature are discussed in Ref. 20 and so will be only summarized here. The time rate of change of charge density in numerical cell  $k$ ,  $\rho_k$  (C/cm<sup>3</sup>) is

$$\frac{d\rho_k}{dt} = \sum_i \frac{q_i w_i}{\Delta V_k} - \nabla \cdot \rho_k \mu_k \vec{E}, \quad (4)$$

where  $\vec{E} = -\nabla\Phi$  is the electric field,  $\Phi$  is the electric potential, and the sum is over incident particles  $i$  having weighting  $w_i$  and carrying charge  $q_i$ . The numerical cell has volume  $\Delta V_k$  and the charge has the electrical mobility  $\mu_k$  in that cell. The electric potential is obtained by implicitly solving Poisson's equation,  $-\nabla \cdot \epsilon \nabla \Phi = \rho$ , using finite volume techniques. Computationally, this is performed using the successive-over-relaxation algorithm employing a parallel red-black technique. Each material included in the simulation is assigned a dielectric constant and mobilities for positive and negative charge transport. The dielectric constants and

mobilities in the computational mesh then vary as the material identities change. Due to the computational expense of solving Poisson's equation, the potential is updated only after 400 charged particles strike a surface. This is a large enough number to provide some computational efficiency, but a small enough number indicating that there are not significant unaccounted for changes in electric potential. (Millions of charged particles are launched during the simulation.)

Reflective boundary conditions for electric potential are used in the lateral (x-y) dimensions and a zero-gradient boundary condition is used on the top surface of the computational domain. The bottom of the computational domain is grounded. In reality, the bottom electrical boundary condition is as far away as the other side of the wafer, which is a distance far greater than what can be resolved in the simulation. However, what is important is that the capacitance of the system is accurately represented. To achieve that end, the dielectric constant of the bottom two to three layers of computational cells above the ground plane is adjusted so that the capacitance of the feature with respect to the ground plane is the same as that for the actual thickness of the wafer.

In the MCFPM, the fluxes of species incident onto the etch front were measured by tallying the number of pseudoparticles that impact an 18 × 18 nm<sup>2</sup> window at the center of the feature at the depth of the lowest point of the feature. The number of impacts of each pseudoparticle representing a given species arriving at the etch front window was scaled by the weight of a single pseudoparticle (the number of atoms or molecules that each pseudoparticle represents), divided by the surface area of the cell collecting the particle and multiplied by the dot product of the vector velocity of the particle and the surface normal at the site of incidence. To reduce the noise while capturing the general trend of the fluxes with increasing aspect ratio, a digital three-point filter with the coefficients of 0.25, 0.5, and 0.25 was used to smooth the fluxes. The etch depth is the vertical distance between the position of the etch front and the position of the interface between SiO<sub>2</sub> and photoresist (PR) at the top of the feature.

All of the initially released particles in the MCFPM were reactive species (e.g., ions, electrons, and neutral radicals) and their trajectories were tracked through several collisions with the surface until the particle was either consumed or left the feature. The reactive etch or sputter products produced by surface reactions (e.g., SiF<sub>x</sub> and CF<sub>x</sub>) were also tracked in the MCFPM, while the nonreactive products (e.g., CO and CO<sub>2</sub>) were not tracked. The fluxes of reactive species out of the feature were measured by counting the number of pseudoparticles leaving the feature passing out of the top of the computational domain. For nonreactive species products of surface reactions, the fluxes out of the feature were accounted for by counting the nonreactive species produced after surface reactions.

### III. SURFACE REACTION MECHANISM FOR SiO<sub>2</sub> ETCHING IN FLUOROCARBON PLASMAS

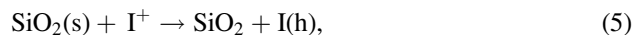
The surface reaction mechanism for the etching of SiO<sub>2</sub> using Ar/C<sub>4</sub>F<sub>8</sub>/O<sub>2</sub> mixtures in MCFPM is an updated version

based on previous studies<sup>38,45</sup> to better address the HAR feature etching process. Listings of the gas phase species, surface sites, and the reactions between gas phase species and surface sites are given in Table I.

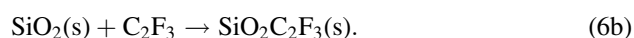
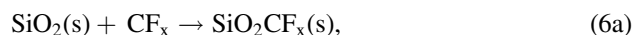
The gas phase reactants are classified into the following categories: (a) Ions, which are typically incident onto the feature with high energies. (b) Hot neutral particles, which are produced by ions having neutralizing collisions with surfaces. Other than their charge, hot neutrals have the same reactive energy dependencies as their corresponding ions. (c) Thermal neutral particles, whose sources are either radicals incident into the feature from the gas phase or hot neutrals that have slowed to thermal energies. (d) Electrons, which in this mechanism are unreactive other than charging surfaces. (e) Unreactive etch products, which are not tracked as pseudoparticles and removed from the simulation while accounting for their fluxes leaving the feature. In the following text, the term *ion* refers to *both incident ions and their hot neutrals* which have the same reaction mechanism.

In what follows, reactions involving fluorocarbon radicals are discussed. These fluorocarbon radicals come in the form of CF, CF<sub>2</sub>, and CF<sub>3</sub>, collectively referred to as CF<sub>x</sub>, and in the form of C<sub>m</sub>F<sub>n</sub>, m > 1. In the absence of fully dissociating the C<sub>4</sub>F<sub>8</sub> feedstock gas, a significant fraction of the C<sub>m</sub>F<sub>n</sub> fluorocarbon radicals incident onto the substrate have only a single dangling bond. In many cases, if there was any finite surface reactivity of these single dangling bond species, there would be overwhelming polymer deposition that would prevent etching for conditions where robust etching is observed. Following extensive parameterization and sensitivity studies, we concluded that reactive C<sub>m</sub>F<sub>n</sub> radicals on surfaces must have at least two dangling bonds. Those having single dangling bonds have restricted reactivity due to steric factors. These multicarbon fluorocarbon radicals having at least two dangling bonds (i.e., C<sub>2</sub>F<sub>3</sub>, C<sub>3</sub>F<sub>5</sub>, and C<sub>3</sub>F<sub>6</sub>) are collectively referred to as C<sub>x</sub>F<sub>y</sub>. For the purpose of describing specific reactions, C<sub>2</sub>F<sub>3</sub> will be used as an example. In recognition of the higher reactivity of CF<sub>x</sub> radicals having more dangling bonds, the following scaling was used. The default probability for a given reaction, *p*, is that for CF<sub>3</sub>. The reaction probability for CF<sub>2</sub> is 1.5*p* and that for CF is 2*p*, where the maximum allowed probability is 0.9. Although this scaling is approximate, it does capture the trends shown in molecular dynamics simulations.<sup>46,47</sup>

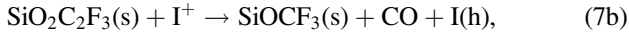
SiO<sub>2</sub> can be directly sputtered by energetic ions through



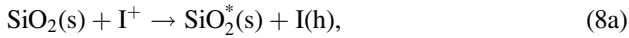
where *s* denotes a surface site, I<sup>+</sup> denotes any ion, and I(h) denotes the hot neutral partner of I<sup>+</sup>. SiO<sub>2</sub> can be chemically removed through two steps. The first step is passivation of a pristine SiO<sub>2</sub> surface by CF<sub>x</sub> and C<sub>x</sub>F<sub>y</sub> to form a passivated layer (complex) through



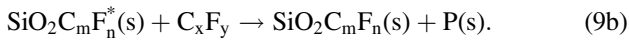
The complex is chemically removed by energetic ions through



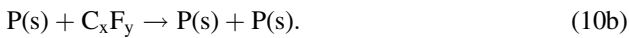
In addition to physical and chemical sputtering, the ions can also activate surface sites through



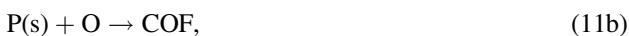
where SiO<sub>2</sub>\*<sub>(s)</sub> denotes the activated oxide surface site, SiO<sub>2</sub>C<sub>m</sub>F<sub>n</sub>(s) denotes the complex, and SiO<sub>2</sub>C<sub>m</sub>F<sub>n</sub>\*<sub>(s)</sub> denotes the activated complex. The CF<sub>x</sub> and C<sub>x</sub>F<sub>y</sub> radicals have higher sticking probabilities on the activated complex sites than on the unactivated complex sites. Deposition of CF<sub>x</sub> on activated sites produce the base layer of polymer P(s) through



Subsequent polymer growth occurs on top of the polymer layer through



The P(s) site can also be ion activated in the same manner as that of SiO<sub>2</sub>C<sub>m</sub>F<sub>n</sub>\*<sub>(s)</sub>. The activated polymer site, P\*(s), has a higher reaction probability than that of the pristine polymer site, P(s). In the following context, P(s) refers to both pristine and activated polymer sites. The polymer can be thermally etched by F and O radicals through

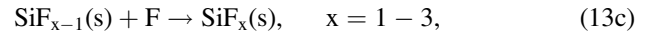
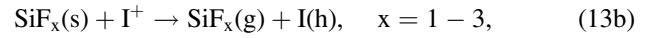


and physically sputtered by energetic ions through



In the etching of SiO<sub>2</sub> in fluorocarbon gas mixtures, the polymer layer plays an important role. Thicker polymer layers result in limited availability of activation energy and reactants to the underlying complex, while thinner polymer layers result in limited amount of fuel for the removal of oxygen surface sites. Thus, controllable polymer deposition and polymer thickness is necessary to optimize the SiO<sub>2</sub> etching process.

In our model geometry, a hydrocarbon PR is the photolithographic mask and Si is the stopping layer underneath SiO<sub>2</sub>. Si can be sputtered by ions or thermally etched by F atoms through



Similarly, PR can also be directly sputtered by energetic ions and thermally etched by O atoms



The sputtered gas phase photoresist fragment, R, can then redeposit on any surface.

#### IV. TRI-FREQUENCY CAPACITIVELY COUPLED PLASMA

A TF-CCP reactor was used as a model system for simulations of etching of HAR features in SiO<sub>2</sub>. TF-CCPs are being developed for HAR etching due to the large dynamic range available for ion energy and angular distributions (IEADs) for process optimization. A schematic of the TF-CCP reactor used in this study is shown in Fig. 1, a design resembling TF-CCPs in use in industry. In this reactor, a 300 mm wafer was placed on the bottom electrode, confined by an Si focus ring. Power at 80 MHz was applied to the top electrode above the Si showerhead, while 10 and 5 MHz powers were applied to the bottom electrode through a blocking capacitor, with all the metal sidewalls being grounded. The gap between the top and the bottom electrodes was 3 cm. The materials in contact with the plasma had fixed temperatures of 333 K except for the wafer and the focus ring which were cooled to 293 K. The secondary electron emission coefficient for ions was 0.15 on the wafer and the focus ring, 0.05 on quartz, and 0.005 on the alumina covering the sidewalls. In the base case, the powers of the 80, 10, and 5 MHz sources were 400, 2500, and 5000 W, respectively. During the execution of the HPEM, the voltage of each frequency was dynamically adjusted to provide the specified power. In the base case, the voltages to deliver the specified powers were 80/10/5 MHz = 125/1030/2450 V, with a dc bias of -1690 V.

Fluorocarbon gas mixtures are usually used in SiO<sub>2</sub> etching to produce CF<sub>x</sub> radicals which are the primary etchants. In this study, the gas mixture was Ar/C<sub>4</sub>F<sub>8</sub>/O<sub>2</sub> = 75/15/10, injected through the showerhead with a total flow rate of 500 sccm (standard cubic centimeters per minute). The gas pressure at the sensor near the foreline was kept at 25 mTorr by adjusting the flow rate leaving through the pump. The species included in the reactor scale model are Ar, Ar(1s<sub>5</sub>), Ar(1s<sub>4</sub>), Ar(1s<sub>3</sub>), Ar(1s<sub>2</sub>), Ar(4p), Ar(4d), Ar<sup>+</sup>, C<sub>4</sub>F<sub>8</sub>, C<sub>4</sub>F<sub>7</sub>, C<sub>3</sub>F<sub>7</sub>, C<sub>3</sub>F<sub>6</sub>, C<sub>3</sub>F<sub>5</sub>,

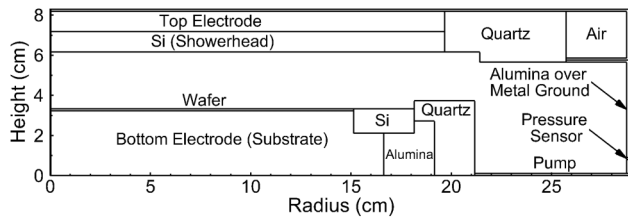


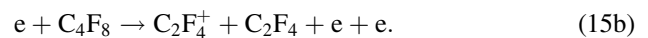
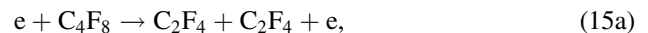
FIG. 1. Schematic of the TF-CCP reactor used in the simulation. 80 MHz power is applied to the top electrode. 10 and 5 MHz powers are applied to the bottom electrode.

C<sub>2</sub>F<sub>6</sub>, C<sub>2</sub>F<sub>5</sub>, C<sub>2</sub>F<sub>4</sub>, C<sub>2</sub>F<sub>3</sub>, CF<sub>4</sub>, CF<sub>3</sub>, CF<sub>2</sub>, CF, C, C<sub>4</sub>F<sub>8</sub><sup>+</sup>, C<sub>4</sub>F<sub>7</sub><sup>+</sup>, C<sub>3</sub>F<sub>7</sub><sup>+</sup>, C<sub>3</sub>F<sub>6</sub><sup>+</sup>, C<sub>3</sub>F<sub>5</sub><sup>+</sup>, C<sub>2</sub>F<sub>5</sub><sup>+</sup>, C<sub>2</sub>F<sub>4</sub><sup>+</sup>, C<sub>2</sub>F<sub>3</sub><sup>+</sup>, CF<sub>3</sub><sup>+</sup>, CF<sub>2</sub><sup>+</sup>, CF<sup>+</sup>, CF<sub>3</sub><sup>-</sup>, F<sub>2</sub>, F, F(<sup>3</sup>S), F<sub>2</sub><sup>+</sup>, F<sup>+</sup>, F<sup>-</sup>, O<sub>2</sub>, O<sub>2</sub>(a <sup>1</sup>Δ<sub>g</sub>), O, O(<sup>1</sup>D), O<sub>2</sub><sup>+</sup>, O<sup>+</sup>, O<sup>-</sup>, CO<sub>2</sub>, CO, FO, COF, SiF<sub>4</sub>, SiF<sub>3</sub>, SiF<sub>2</sub>, SiF, and electrons. A detailed description of the Ar/C<sub>4</sub>F<sub>8</sub>/O<sub>2</sub> gas phase reaction mechanism is given in Refs. 48 and 49.

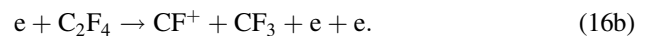
The time averaged electron density, ionization source by bulk electrons,  $S_b$ , ionization source by secondary electrons,  $S_s$ , and electron temperature,  $T_e$ , for the base case are shown in Fig. 2. The electron density has an edge-high profile and peaks at  $3.8 \times 10^{10} \text{ cm}^{-3}$  at the outer radius of the wafer due to electric field enhancement at the triple point composed of the wafer, focus ring, and plasma. (No attempt was made to optimize the uniformity of the plasma or fluxes to the wafer in this system.) The ionization by bulk electrons is the dominant

source of electrons, which also peaks at the edge of the wafer at  $5.3 \times 10^{15} \text{ cm}^{-3} \text{ s}^{-1}$ . The contribution of ionization by secondary electrons is about one-fifth of the bulk electrons. However, the ionization source by secondary electrons is quite uniform at the wafer surface with a rate of  $1.2 \times 10^{15} \text{ cm}^{-3} \text{ s}^{-1}$  due to the ion bombardment of the surface, which improves the uniformity of the plasma density in the radial direction. The electron temperature in the bulk plasma is 4 eV, which is a typical value for electronegative plasmas to provide ionization sources to balance attachment. The time averaged thickness of the sheath at the wafer surface is about 0.8 cm due to the high bias voltage. This thick sheath is mildly collisional. (The thickness of the sheath is determined by the distance between the electrode surface and the position where the densities of electrons and ions begin to deviate.)

Fluxes of radicals and ions to the wafer surface for the base case are shown in Fig. 3. The feedstock C<sub>4</sub>F<sub>8</sub> gas is dissociated dominantly by electron impact reactions to produce fluorocarbon radicals and ions, resulting in a fractional dissociation of about 24%. The dominant electron impact dissociation product is C<sub>2</sub>F<sub>4</sub>, which is produced by



Although C<sub>2</sub>F<sub>4</sub> is not particularly reactive in oxide etching, further dissociation of C<sub>2</sub>F<sub>4</sub> produces CF<sub>x</sub> radicals and ions



CF<sub>2</sub> and CF<sub>3</sub> are the dominant reactive fluorocarbon species incident onto the wafer with average fluxes of  $1.4 \times 10^{17}$  and  $0.9 \times 10^{17} \text{ cm}^{-2} \text{ s}^{-1}$ , respectively. O and F atoms are mainly produced through electron impact dissociation of O<sub>2</sub> and CF<sub>x</sub> species and diffuse to the wafer with average fluxes of  $1.2 \times 10^{17}$  and  $0.8 \times 10^{17} \text{ cm}^{-2} \text{ s}^{-1}$ , respectively.

Fluxes of ions to the wafer surface are lower than those of radicals by 1–2 orders of magnitudes due to the higher activation energy required for ionization than for dissociation. Ar<sup>+</sup> has the highest flux to the wafer of  $3.9 \times 10^{15} \text{ cm}^{-2} \text{ s}^{-1}$  due to the large mole fraction (75%) of the parent Ar. There is also a significant flux of C<sub>2</sub>F<sub>4</sub><sup>+</sup> ( $2.0 \times 10^{15} \text{ cm}^{-2} \text{ s}^{-1}$ ) due to the large dissociation fraction of C<sub>4</sub>F<sub>8</sub> producing a large volume averaged density of C<sub>2</sub>F<sub>4</sub> ( $3.2 \times 10^{13} \text{ cm}^{-3}$ ). The densities of C<sub>2</sub>F<sub>4</sub><sup>+</sup> and C<sub>3</sub>F<sub>5</sub><sup>+</sup> are larger than the densities of CF<sup>+</sup>, CF<sub>2</sub><sup>+</sup>, and CF<sub>3</sub><sup>+</sup> by 1 order of magnitude. In high plasma density sources, such as inductively coupled plasmas, the majority of power is coupled into the electrons producing electron densities that are typically 10–100 times higher than in CCPs, while the gas pressures are lower. This results in a higher fractional dissociation of feedstock gases and the dominant radicals and ions being CF<sub>x</sub> and CF<sub>x</sub><sup>+</sup>. In CCPs of the type discussed here, the majority of the power is dissipated in the sheath as ion acceleration, with only about 20% of the power being coupled into the electrons. The end result

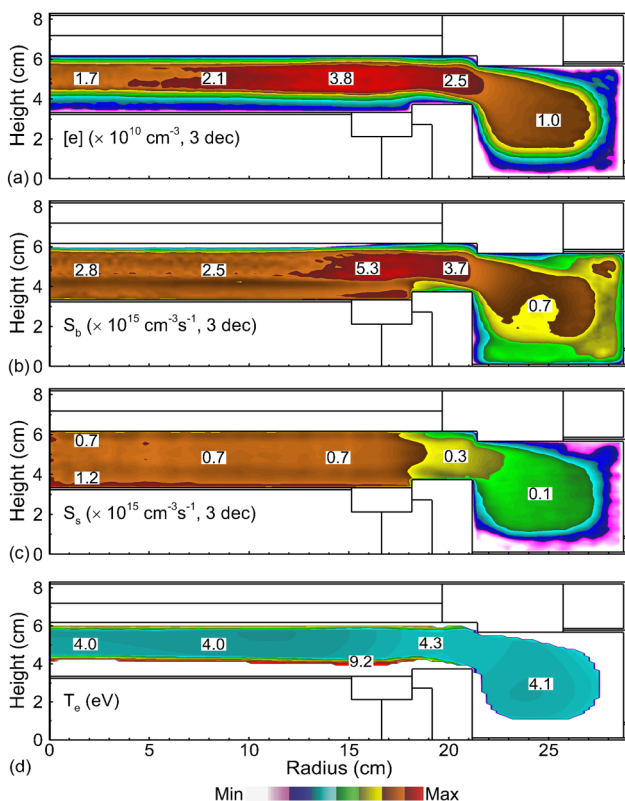


FIG. 2. Time averaged (a) electron density, (b) ionization source by bulk electrons, (c) ionization source by secondary electrons, and (d) electron temperature in a TF-CCP sustained in an Ar/C<sub>4</sub>F<sub>8</sub>/O<sub>2</sub> mixture. (Operating conditions: Ar/C<sub>4</sub>F<sub>8</sub>/O<sub>2</sub> = 75/15/10, 25 mTorr, 500 sccm, 80/10/5 MHz power = 0.4/2.5/5 kW.)

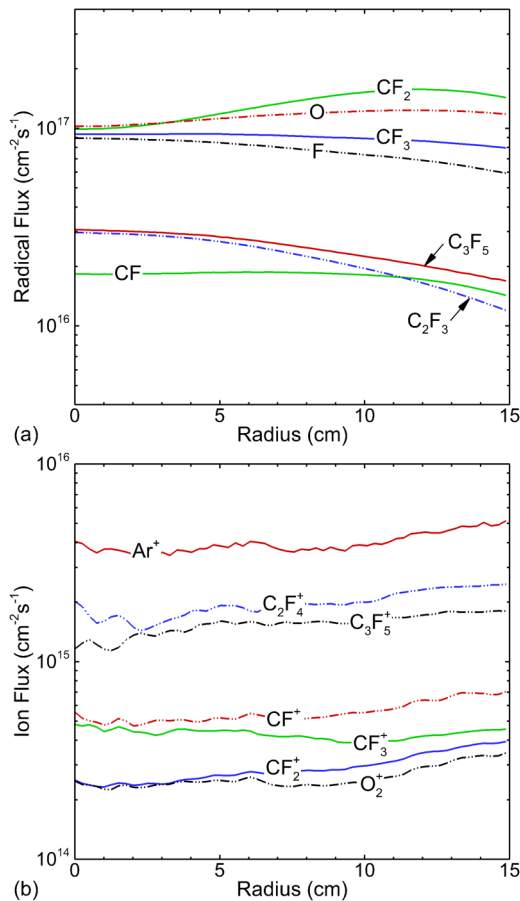


FIG. 3. Time averaged fluxes of (a) radicals and (b) ions to the wafer in a TF-CCP sustained in an Ar/C<sub>4</sub>F<sub>8</sub>/O<sub>2</sub> mixture. (Operating conditions: Ar/C<sub>4</sub>F<sub>8</sub>/O<sub>2</sub> = 75/15/10, 25 mTorr, 500 sccm, 80/10/5 MHz power = 0.4/2.5/5 kW.)

is a lower fractional dissociation of the feedstock gases and larger densities of C<sub>x</sub>F<sub>y</sub> and C<sub>x</sub>F<sub>y</sub><sup>+</sup> than of CF<sub>x</sub><sup>+</sup>, which would require multiple electron collisions to produce.

A parametric study of the TF-CCP was performed by varying the lowest 5 MHz power from 2.5 to 10 kW. The rationale for this choice is that 5 MHz power is dominantly dissipated by ion acceleration in the sheath (compared with 10 and 80 MHz) and so has the most significant effect on IEADs to the wafer of the three frequencies. The time averaged IEADs of all the positive ions, the fluxes of ions and radicals, and the average energy of ions to the wafer at radius of 7.5 cm for different 5 MHz powers are shown in Fig. 4. The IEADs have multiple peaks, which are due to the sheath having components of all three frequencies and a large range of ion masses (16–200 amu). As the 5 MHz power increases from 2.5 to 10 kW, the 5 MHz voltage to deliver the power increases from 1590 to 3430 V, while the dc bias increases from –1450 to –2250 V. These increases in voltage produce an extended IEAD having average ion energies from 1630 eV (2.5 MHz) to 2540 eV (10 MHz) and maximum energies of 2300–4000 eV. The IEAD becomes narrower in angle (incident angle of ions is less than 3° with respect to surface normal) with increasing 5 MHz power due to the increasing acceleration of ions in the sheath perpendicular to the wafer,

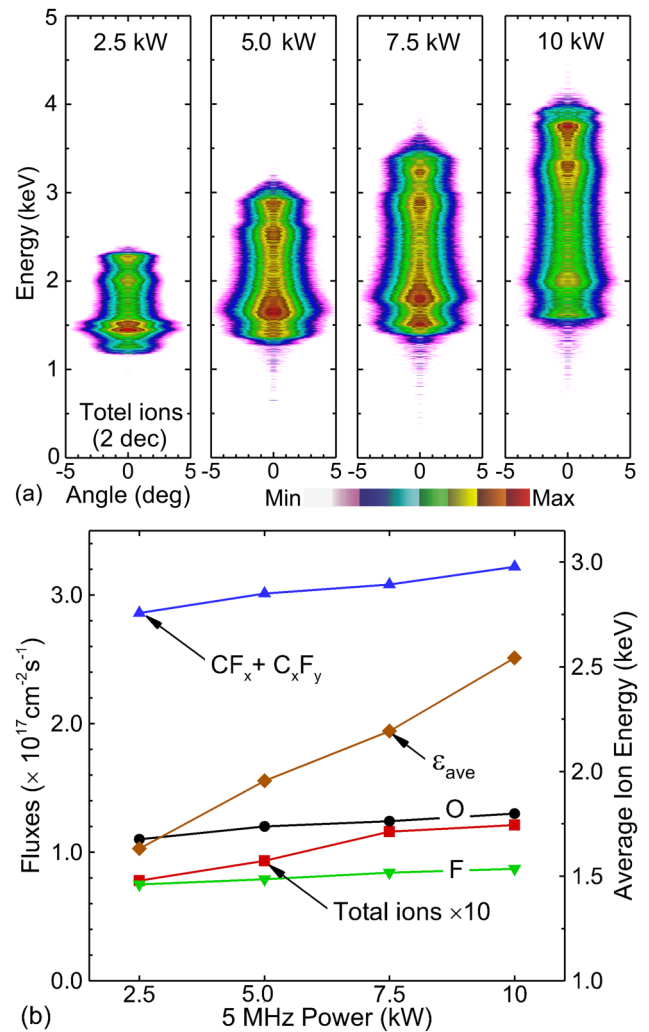


FIG. 4. Properties of fluxes to the wafer. (a) IEADs of all positive ions and (b) fluxes of ions and radicals and average energy of ions reaching the wafer at a radius of 7.5 cm for different 5 MHz powers. (Operating conditions: Ar/C<sub>4</sub>F<sub>8</sub>/O<sub>2</sub> = 75/15/10, 25 mTorr, 500 sccm, 80/10 MHz power = 0.4/2.5 kW, 5 MHz power: 2.5–10 kW.)

a desirable trend in HAR etching to reduce sidewall impacts in the feature and produce anisotropic etch profiles.

The thickness of the sheath at the surface of the wafer increases from 0.8 to 1.0 cm as the 5 MHz power increases from 2.5 to 10 kW, as the overall waveform and amplitude of the sheath is dominantly modulated by the 5 MHz power. The narrowing of the angular spread of the IEAD is somewhat less than what one would expect by increasing the applied voltage by more than a factor of 2. Assuming collisionless acceleration of ions through the sheath, the angular spread of the IEADs striking the wafer should scale as  $\Delta\theta \sim (T_{ion}/V_S)^{1/2}$ , where  $V_S$  is the average sheath potential and  $T_{ion}$  is the ion temperature parallel to the sheath edge. If the plasma density remains constant, then the sheath thickness increases as  $\lambda_S \sim V_S^{1/2}$ . The thicker sheath enables more glancing angle elastic collisions, which increases the effective value of  $T_{ion}$ . The end result is that if the sheath (or pre-sheath) is mildly collisional,  $\Delta\theta$  does not decrease with  $V_S$  as intended. To maintain that scaling, the  $\lambda_S$  should remain

constant, which would then require that the electron density  $n_e \sim V_S$ . For low frequency biases whose power is dominantly dissipated by ion acceleration, there is little change in  $n_e$  with  $V_S$ . Maintaining a constant sheath thickness with increasing  $V_S$  requires a corresponding increase in high frequency source power.

As the 5 MHz power increases from 2.5 to 10 kW, the total flux of all positive ions to the wafer at a radius of 7.5 cm increases by about 50%, from  $0.8 \times 10^{16}$  to  $1.2 \times 10^{16} \text{ cm}^{-2} \text{ s}^{-1}$ . This increase in ion fluxes results from an increase in the volume averaged ionization source by bulk electrons between the electrodes from  $2.3 \times 10^{15}$  to  $5.0 \times 10^{15} \text{ cm}^{-3} \text{ s}^{-1}$ , and a thickening of the sheath and presheath which captures more of the ion generation into the wafer directed ion flux. The volume averaged electron density increases from  $0.8 \times 10^{10}$  to  $1.0 \times 10^{10} \text{ cm}^{-3}$  with increasing 5 MHz power, resulting in a moderate increase in dissociation rates, which increase fluxes of CF<sub>x</sub> and C<sub>x</sub>F<sub>y</sub> from  $2.9 \times 10^{17}$  to  $3.2 \times 10^{17} \text{ cm}^{-2} \text{ s}^{-1}$ .

## V. ETCHING PROFILE OF HIGH ASPECT RATIO CONTACTS IN SiO<sub>2</sub>

The features we are investigating are simple circular vias. The geometry of the three-dimensional high HAR via in SiO<sub>2</sub> is shown in Fig. 5. The thickness of SiO<sub>2</sub> is 4800 nm, with a 1600 nm thick PR layer as the mask and Si as the stopping layer below SiO<sub>2</sub>. The diameter of the mask opening in the PR is 120 nm. The mask initially has beveled edges with an angle of 45° and a depth of 60 nm. The mask is otherwise azimuthally smooth. That is, in this study, we are not considering the consequences of innate line-edge roughening of the mask. The mesh consisted of  $60 \times 60 \times 1094$  cells, producing cubic voxels 6 nm on a side. The AR is defined by the PR mask opening divided by the etch depth in the oxide, so the AR of the feature in oxide is 40. The total aspect ratio including the mask at the start of etching is 53. Unless otherwise stated, the aspect ratio in the following context denotes the aspect ratio of the feature only in the oxide. Charging is not considered in etching the features discussed here and in Secs. V A–V C. Charging of features is discussed in Sec. V D.

Although not a focus of this paper, two-dimensional simulations (e.g., infinite trenches) are often used to approximate vias. As part of this and related investigations, we have performed side-by-side comparisons of the simulations of trenches and vias. Although quantitative systematic trends are difficult to discern, there are clearly differences in the resulting profiles. These differences in large part result from the difference in the effective surface-to-volume (SVR) ratio of the features—the SVR is higher in the via than in the trench. The higher SVR of the vias results in sidewall scattering and deposition on the sidewalls being more important in the vias compared with the trench. We also found that simulating a trench in 2D produces somewhat different results than simulating a trench in 3D. The 3D trench would be simulated, for example, by having a finite depth to the computational mesh with periodic boundary conditions. This difference between 2D trenches and 3D trenches is

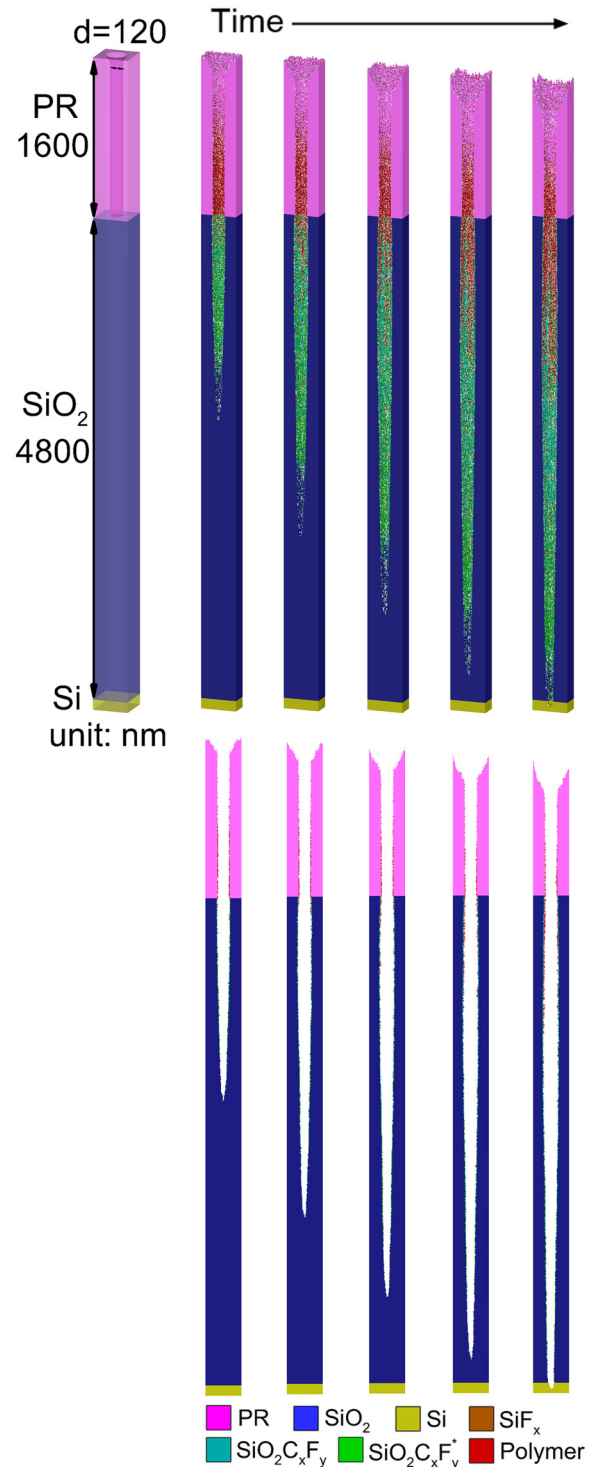


Fig. 5. HAR feature etching properties. Section view (top) and central slice (bottom) of the HAR feature showing the time evolution of the etch profile. The height of SiO<sub>2</sub> is 4800 nm with a 1600 nm thick photoresist as the mask and Si as the stopping layer. (Operating conditions: Ar/C<sub>4</sub>F<sub>8</sub>/O<sub>2</sub> = 75/15/10, 25 mTorr, 500 sccm, 80/10/5 MHz power = 0.4/2.5/5 kW.)

particularly evident when including charging. This difference results from roughness (or charge) on the sidewall in 2D appearing to have an infinite depth, whereas roughness (or charge) on the sidewall in 3D has a finite extent. Scattering from sidewall roughness in 2D trenches will

occur from the same height for all particles. Scattering from sidewall roughness in 3D will be more statistical since the roughness is not uniform along the depth of the trench.

Using fluxes and IEADs obtained from the reactor scale base case, the time evolution of etching the via is shown in Fig. 5. These images are 3D cutout views and 2D sectional slices taken through the middle of the feature. The bottoms of the 2D sectional slices are not symmetric across the centerline, an indication of pattern distortion which will be discussed below. As the etching proceeds, there is tendency toward bowing in the upper portion of the feature in SiO<sub>2</sub> for etch depths of 200–1200 nm (AR of 2–10). The bowing is largely due to diffusive scattering of ions at the sidewalls of the PR and to a lesser degree from inside the feature. This diffusive scattering produces hot neutrals at large angles. Also, the erosion of the PR results in increasing the area of the facet at the top of PR, and scattering of ions at the facet produces hot neutrals into the feature with broad angular distributions. For reflections from the facets to be a direct source of bowing in SiO<sub>2</sub>, there should be a line of sight from the facet to the top of SiO<sub>2</sub>, which is not the case here. Reflections from the facets here broaden the angular distribution for subsequent sidewall collisions. The PR has been eroded by approximately 450 nm by the end of the etch when the feature reaches the Si stopping layer, yielding a selectivity of SiO<sub>2</sub> over a PR of 10.7.

The fluxes of ions, hot neutrals, CF<sub>x</sub>, and C<sub>x</sub>F<sub>y</sub> radicals incident onto the etch front as a function of the aspect ratio of SiO<sub>2</sub> and of the total feature (PR + SiO<sub>2</sub>) as the feature etches are shown in Fig. 6(a). The average energies and power flux striking the etch front by ions and hot neutrals are shown in Fig. 6(b). By definition, ions striking the etch front are those not having had collisions with the sidewalls as, in this mechanism, ions neutralize upon striking a surface and become hot neutrals. A given ion can strike the etch front only once, so the flux of ions to the etch front to some degree represents the decreasing view angle of the etch front subtending the ion angular distribution at that AR. For this reason alone, the ion flux to the etch front decreases with AR. On the other hand, thermal neutral species undergoing diffusive scattering on the sidewalls are conductance limited in reaching the etch front as the AR increases. If a neutral has a nonunity reaction probability, once at the bottom of the feature, that particle can strike the etch front multiple times. Each strike of the etch front by a neutral particle (either hot or thermal) increments the flux count.

Even at low aspect ratio in SiO<sub>2</sub>, the flux of hot neutrals to the etch front is nearly the same as that of ions. This equivalence results from the PR itself having an AR of 13, so, there is considerable scattering of ions from the sidewalls of the PR, with hot neutrals being the returning species at the start of etching. This scaling is demonstrated in Fig. 7 where the fluxes of ions and hot neutrals to the top of SiO<sub>2</sub> at the start of etching are shown as a function of the height of the PR. As the height of the PR increases from 0 to 2400 nm and the aspect ratios of the PR from 0 to 20, the flux of ions to the etch front monotonically decreases ( $4.2 \times 10^{15}$  to  $1.3 \times 10^{15} \text{ cm}^{-2} \text{ s}^{-1}$ ), while the flux of hot neutrals increases (0 to  $2.9 \times 10^{15} \text{ cm}^{-2} \text{ s}^{-1}$ ). With increasing AR of the PR

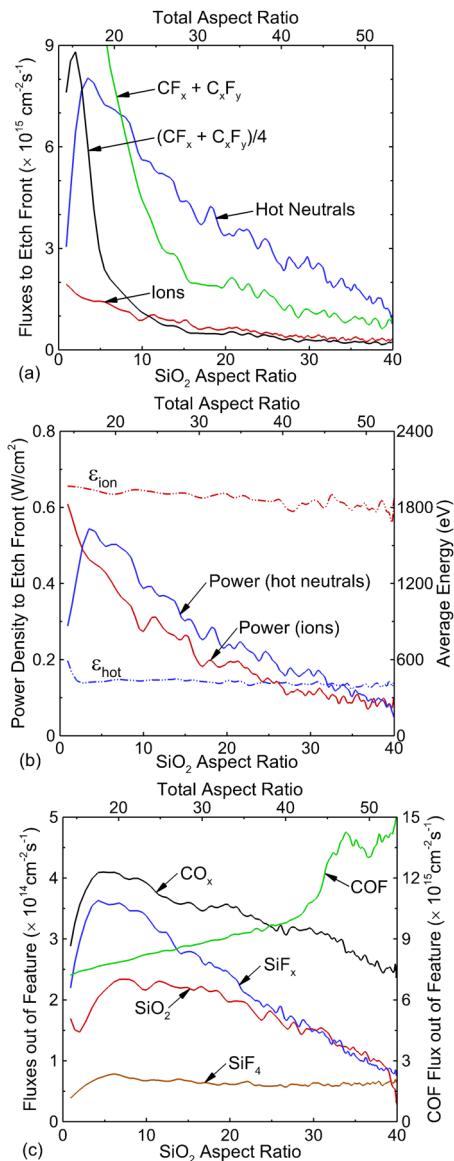


Fig. 6. Fluxes and powers to the etch front as a function of aspect ratio. (a) Fluxes of ions, hot neutrals, and CF<sub>x</sub> and C<sub>x</sub>F<sub>y</sub> radicals to the etch front, (b) power delivered to the etch front by ions and hot neutrals and the average energy of ions and hot neutrals to the etch front, and (c) fluxes of etch products leaving the feature as a function of the aspect ratio in HAR during etching. (Operating conditions: Ar/C<sub>4</sub>F<sub>8</sub>/O<sub>2</sub> = 75/15/10, 25 mTorr, 500 sccm, 80/10/5 MHz power = 0.4/2.5/5 kW.)

above SiO<sub>2</sub>, more ions are neutralized on the sidewalls of the PR producing hot neutrals before reaching the SiO<sub>2</sub> surface.

For the base case having PR with an AR of 13, with etching into SiO<sub>2</sub> increasing the overall AR, sidewall scattering continually depletes ions converting them to hot neutrals, as shown in Fig. 6(a). (Recall that hot neutrals are those particles having energies as high as specularly reflected ions to as low as a few eV.) After converting ions to hot neutrals (including possible multiple collisions of hot neutrals with the etch front), there is a rapid increase in the hot neutral flux for an AR up to about 4 (or about 17 from the top of the PR). At larger AR, multiple scattering of the hot neutrals from the sidewalls reduces their energy. Reflections from the sidewalls can also include a stochastic diffusive component in the

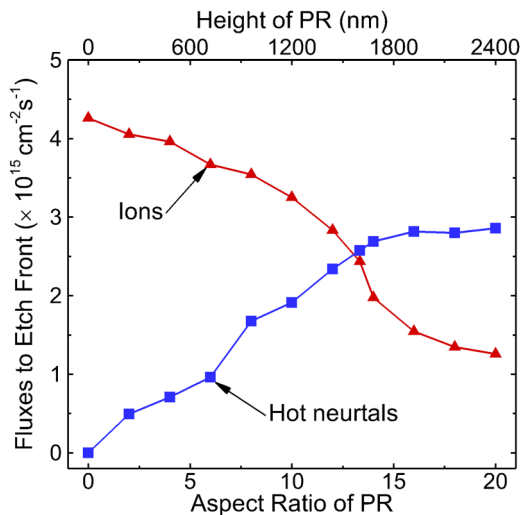


FIG. 7. Instantaneous etch rates of oxide and photoresist as a function of aspect ratio in HAR etching. (Operating conditions: Ar/C<sub>4</sub>F<sub>8</sub>/O<sub>2</sub> = 75/15/10, 25 mTorr, 500 sccm, 80/10/5 MHz power = 0.4/2.5/5 kW.)

reflected velocity.<sup>50</sup> This results in a more isotropic velocity distribution as the average number of reflections increases and energy decreases. As the initially anisotropic hot neutrals become more isotropic, conduction limits begin to dominate and their fluxes to the etch front decrease with increasing AR.

As the etch depth increases up to 4800 nm and AR = 40 (AR = 53 from top of PR), the maximum incident angle of an ion that can directly hit the etch front without first colliding with the sidewall decreases from about 4° to 1° (with PR included). This shadowing contributes to a decrease in the ion flux to the etch front from  $2.0 \times 10^{15}$  to  $0.3 \times 10^{15} \text{ cm}^{-2} \text{ s}^{-1}$ . The ions that do not directly reach the etch front are neutralized at the sidewall, charging the surface, and are converted to hot neutral partners with mostly specular reflection. The flux of hot neutrals to the etch front increases from  $3.1 \times 10^{15}$  to  $8.0 \times 10^{15} \text{ cm}^{-2} \text{ s}^{-1}$  as the etch depth increases from 0 to 480 nm (AR = 4). As the feature deepens to 960 nm (AR = 8), the flux of hot neutrals surpasses the fluxes of thermal CF<sub>x</sub> and C<sub>x</sub>F<sub>y</sub> radicals whose fluxes are conductance limited. The hot neutral flux then becomes the dominant neutral species reaching the etch front. This initial increase in the flux of hot neutrals is mainly due to more ions striking sidewalls and being converted to hot neutrals; however, there is also a component due to the etch front evolving from a flat to a tapered profile. The tapered feature produces some focusing of specularly reflected hot particles toward the etch front. As the etch depth increases from 480 to 4800 nm (AR = 40), the flux of hot neutrals to the etch front decreases to  $1.1 \times 10^{15} \text{ cm}^{-2} \text{ s}^{-1}$ , which is due to diffusive scattering from the sidewalls and thermalization of the hot particles following several collisions with the surfaces. The average energy of hot neutrals reaching the etch front first decreases with increasing AR and is then maintained at about 400 eV at ARs higher than 3.

The flux of CF<sub>x</sub> and C<sub>x</sub>F<sub>y</sub> to the top of the PR is  $3.0 \times 10^{17} \text{ cm}^{-2} \text{ s}^{-1}$ , resulting in polymer deposition on the top and sidewalls of the PR. This polymer deposition provides some protection of the PR from lateral etching.

In addition to energetic species (i.e., hot neutrals and ions), the chemical etching of SiO<sub>2</sub> depends on the availability of neutral radicals. The incident thermal neutrals have isotropic angular distributions and the delivery of neutrals deep into the feature is limited by gas conductance. As the etch depth increases from 0 to 1200 nm (AR = 10), the flux of CF<sub>x</sub> and C<sub>x</sub>F<sub>y</sub> radicals to the etch front decreases from  $3.1 \times 10^{16}$  to  $0.4 \times 10^{16} \text{ cm}^{-2} \text{ s}^{-1}$ . This decrease is due to consumption by deposition as polymer on the sidewalls and diffusive scattering which reflects the neutrals out of the feature before reaching the etch front (neutral conduction limit). Recall that neutral particles that have nonunity reaction probabilities can strike the etch front several times and are counted with every strike.

The oxide sidewalls of the feature are first passivated by fluorocarbon radical to form the SiO<sub>2</sub>C<sub>m</sub>F<sub>n</sub> surface complexes. The complex layer is then activated by hot neutrals and ions, which leads to the activated complex having a higher probability for CF<sub>x</sub> and C<sub>x</sub>F<sub>y</sub> to deposit as polymer. The polymer deposition on sidewalls reduces the lateral etching by scattered hot neutrals and so reduces the bowing, enabling more directional etching and anisotropic profiles. As the etch depth further increases from 1200 to 4800 nm (AR from 10 to 40), the flux of CF<sub>x</sub> and C<sub>x</sub>F<sub>y</sub> radicals to the etch front decreases from  $4.4 \times 10^{15}$  to  $0.9 \times 10^{15} \text{ cm}^{-2} \text{ s}^{-1}$ , resulting in a surface complex layer with little overlying polymer at the etch front. Due to the limited availability of CF<sub>x</sub> and C<sub>x</sub>F<sub>y</sub> to thicken the polymer, the polymer is rapidly removed by ions and hot neutrals. Deep in the feature (AR > 10), the ions and hot neutrals have larger fluxes to the etch front than those of CF<sub>x</sub> and C<sub>x</sub>F<sub>y</sub> by a factor of 2–3.

For an AR greater than 3 (or an AR about 16 from the top of the PR), the delivery of power to the etch front relies more on the hot neutral flux than on the ion flux, as shown in Fig. 6(b). The power density is calculated as the sum of the fluxes of energetic particles multiplied by the average energy of that species at the etch front. The power density delivered by hot neutrals to the etch front is larger than the ions by about 20% for AR > 3. The ions initially incident into the feature have energies ranging between 1300 and 3000 eV with an average energy of 1950 eV and incident angles of less than 4°, as shown in Fig. 4. Since ions are counted as striking the etch front only if they have not had a collision with the sidewall, the average energy of the ions reaching the etch front shown in Fig. 6(b) is nearly constant at 1900 eV, approximately the average energy of incident ions. The small decrease in ion energy with AR results from the method of sampling and the tapering of the feature. If the bottom of the feature was absolutely flat with straight sidewalls, the average ion energy striking the etch front would increase with AR (subtending a smaller angle) since the higher energy ions have a narrow angular distribution as shown in Fig. 4(a). However, as the etch front tapers, more ions intersect the tapered sidewalls, which preferentially sample ions with a broader angular distribution having, on average, lower energies. With the average ion energy being nearly constant while the ion flux decreases, the power flux to the etch front monotonically decreases.

The average energy delivered to the etch front by hot neutrals only slightly decreases as the flux of neutrals to the etch

front decreases with increasing AR, indicating that the energy delivery is dominated by hot neutrals having only one or two scatters from the sidewall. With the typical bowed geometry of an HAR feature, the first and second scattering events are usually small angle, occurring on the same side of the feature. With each reflection with a less grazing angle of incidence, the angle at which the particle leaves the surface generally increases. Eventually, this angle will increase to the point that the particle traverses the width of the feature and interacts with the opposite side. Due to the bowing, once the particle traverses the feature, its next impact is often closer to being normal than the first grazing reflections. With the impact angle dependent energy loss described in Eq. (3), these interactions reduce the energy of the hot particle to the point that the particle will no longer be tracked as a hot neutral species, but rather as its thermal neutral partner. The decrease in power delivery to the etch front with increasing AR is a major source of ARDE.

The neutral conductance in HAR features affects etching in at least two ways. The first is to limit the delivery of neutral precursors to the etch front. The second is to impede the flow of etch products from deep inside of the feature out of the feature. The conductance limited transport of etch products out of the feature results in redeposition deep inside the feature. The fluxes of gas phase etch products leaving the feature as a function of the aspect ratio as the etch proceeds are shown in Fig. 6(c). At low AR (<10), the removal of oxide is mainly through passivation by CF<sub>x</sub> and C<sub>x</sub>F<sub>y</sub> radicals [Eq. (6)] followed by chemical sputtering by energetic species [Eq. (7)]. At these depths, there are abundant polymerizing CF<sub>x</sub> and C<sub>x</sub>F<sub>y</sub> fluxes. The etch rate is mainly limited by the availability of energetic species, that is, ion limited. The silicon surface sites are mainly removed by the formation of SiF<sub>x</sub> (x = 1–3) as there is an ample F atom flux and subsequent removal through chemical sputtering by energetic particles. The flux of SiF<sub>x</sub> leaving the feature has a dependence on AR that is similar to that of the fluxes of hot neutrals and ions to the etch front shown in Fig. 6(a). This exiting flux of SiF<sub>x</sub> peaks at a depth of 480 nm (AR = 4) at  $3.6 \times 10^{14} \text{ cm}^{-2} \text{ s}^{-1}$ .

At low ARs (<10), the oxide surface sites are mainly removed by the forming CO<sub>x</sub> (x = 1, 2) and COF species through chemical sputtering of the complex by energetic species. With increasing AR, both the fluxes of SiF<sub>x</sub> (etch products of silicon sites) and CO<sub>x</sub> (etch products of oxygen sites) decrease. The CO<sub>x</sub> flux decreases less than the SiF<sub>x</sub> flux as the CO<sub>x</sub> species are nonreactive (in this mechanism) and leave the feature without further reactions. On the other hand, the SiF<sub>x</sub> species can redeposit on the sidewalls and the etch front, which contributes to a tapering of the feature and a slowing of the etch rate (increasing ARDE). Thermal etching of SiF<sub>x</sub> species is also possible by further fluorine exposure, generating an SiF<sub>4</sub> etch product. This product is volatile and does not participate in redeposition, but this pathway is not important for these conditions.

The flux of gas phase SiO<sub>2</sub> exiting the feature indicates the amount of oxide directly removed by physical sputtering through SiO<sub>2</sub>(s) + I<sup>+</sup> → SiO<sub>2</sub> + I(h). For simplicity, the sputtered oxide is treated as a gas phase SiO<sub>2</sub> species as opposed

to separately sputtering as Si and O atoms. This sputtered SiO<sub>2</sub> can redeposit on surfaces or leave the feature into the plasma. The flux of O atoms entering the feature is many orders of magnitude larger than the flux of physical sputtering products exiting the feature; and so, ignoring the O atoms as a physical sputtering product is likely not important. The flux of gas phase SiO<sub>2</sub> exiting the feature reaches a maximum at a depth of 960 nm (AR = 8) with a flux of  $2.3 \times 10^{14} \text{ cm}^{-2} \text{ s}^{-1}$ , decreasing to  $0.5 \times 10^{14} \text{ cm}^{-2} \text{ s}^{-1}$  as the etch depth increases to 4800 nm (AR = 40). At low ARs (<10), the etching of oxide mainly occurs through chemical sputtering due to the large supply of CF<sub>x</sub> and C<sub>x</sub>F<sub>y</sub> radicals. As the AR increases above 8, the fractional decrease in the flux of gas phase SiO<sub>2</sub> out of the feature is smaller than for the chemical sputtering etch products. With increasing AR, the flux of SiO<sub>2</sub> out of the feature approaches the fluxes of CO<sub>x</sub> and SiF<sub>x</sub>, indicating an increasing fractional contribution of physical sputtering and decreasing fractional contribution of chemical sputtering to the removal of oxide.

Overall, the ratio of oxide removed by chemical sputtering compared with physical sputtering is 1.9 (measured by the ratio of passivated etch product SiF<sub>x</sub> compared with the SiO<sub>2</sub> etch product). The flux of COF leaving the feature increases from  $0.7 \times 10^{16}$  to  $1.5 \times 10^{16} \text{ cm}^{-2} \text{ s}^{-1}$  as the AR increases from 0 to 40. In addition to being formed through chemical sputtering of the SiO<sub>2</sub>C<sub>m</sub>F<sub>n</sub> complex, COF is also formed through etching of polymer by gas phase oxygen species (O, O<sup>+</sup>, and O<sub>2</sub><sup>+</sup>). Polymer etching by O containing species becomes the major source of COF at high ARs due to there being a more polymer covered surface on the sidewalls with increasing AR.

The instantaneous etch rate of SiO<sub>2</sub> as a function of AR shown in Fig. 8 shows typical ARDE: decreasing etch rate with increasing etch depth or aspect ratio. The instantaneous etch rate is calculated by measuring the average height of the solid surface in a 18 × 18 nm window at the

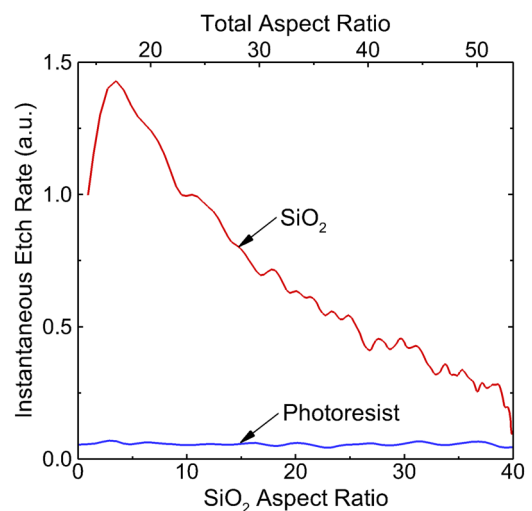


Fig. 8. Fluxes of ions and hot neutrals to the etch front at the beginning of the etching process for SiO<sub>2</sub> features while varying the height of the PR from 0 to 2400 nm. The diameter of initial mask opening in the PR is 120 nm. (Operating conditions: Ar/C<sub>4</sub>F<sub>8</sub>/O<sub>2</sub> = 75/15/10, 25 mTorr, 500 sccm, 80/10/5 MHz power = 0.4/2.5/5 kW.)

center of the feature for equally spaced time steps and taking the first order derivative of the height with respect to time. The instantaneous etch rates were normalized by setting the initial etch rate to 1. There is a small initial increase in the etch rate which is due to the tapering of the feature that funnels hot neutrals to the etch front. The etch rate then decreases by 80% by the time the AR reaches 40, following a trend that is similar to that of the fluxes and power densities of energetic species to the etch front shown in Figs. 6(a) and 6(b). This correlation results from the propagation of the etch front ultimately being driven by energetic species through physical and chemically enhanced sputtering. With the delivery of both energetic species and power to the etch front decreasing with increasing AR, the etch rate decreases, resulting in ARDE. There is also a contribution to ARDE from a redeposition of etch products; however, the more dominant source of ARDE is the reduction in power to the etch front.

The instantaneous etch rate of the PR shown in Fig. 8 is nearly independent of AR and is about 0.05 that of the initial oxide etch rate. Any changes in the PR etch rate are due to the erosion of the PR which results in ions striking the surface at non-normal (top surface) or nongrazing (side surface) angles, or a redeposition of etch products. With the decrease in the oxide etch rate due to ARDE, the selectivity (oxide etch rate/PR etch rate) decreases with increasing AR. The end result is that the relative rate of PR erosion increases as the AR increases, as shown in Fig. 5. This decreasing PR selectivity is a limiting factor in etching HAR features, motivating the use of hard non-eroding masks. For example, for the base case conditions, the PR mask is nearly fully eroded when reaching an AR of 60, as shown in Fig. 9. This loss of selectivity is not because the PR etches faster, but rather because the SiO<sub>2</sub> etches slower. There is a counterintuitive positive contribution to the mask erosion. With thick masks having a finite AR before reaching the top surface of SiO<sub>2</sub>, there is already some conductance limit to transport of neutral radicals and sidewall scattering of ions, both of which contribute to ARDE. As the mask erodes, the conductance limit of neutrals into the SiO<sub>2</sub> portion of the feature relaxes and the unimpeded ion flux to the etch front increases. ARDE would be even more severe in the absence of PR erosion.

Having said that, there are several negative consequences of the mask erosion, including bowing of the via below the mask. The bowing results from ion reflection from the PR which produces energetic hot neutrals at nongrazing angles incident onto the sidewalls of the via below the mask. These trends have also been seen in previous studies in Refs. 2 and 6. These nongrazing particles are produced either directly from reflection off the facets or sidewalls of the PR or following several reflections from the sidewalls of the PR. As the mask is eroded, the likelihood for a direct line-of-sight reflection from the facet into the feature increases, thereby increasing the likelihood for bowing.

To examine the consequences of PR erosion, the probabilities of physical sputtering of PR by energetic ions,  $R(s) + I^+ \rightarrow R + I(h)$ , and thermal etching of PR by O atoms,  $R(s) + O \rightarrow COH$ ,  $a_0$ , were both decreased to 50%, 25%, and

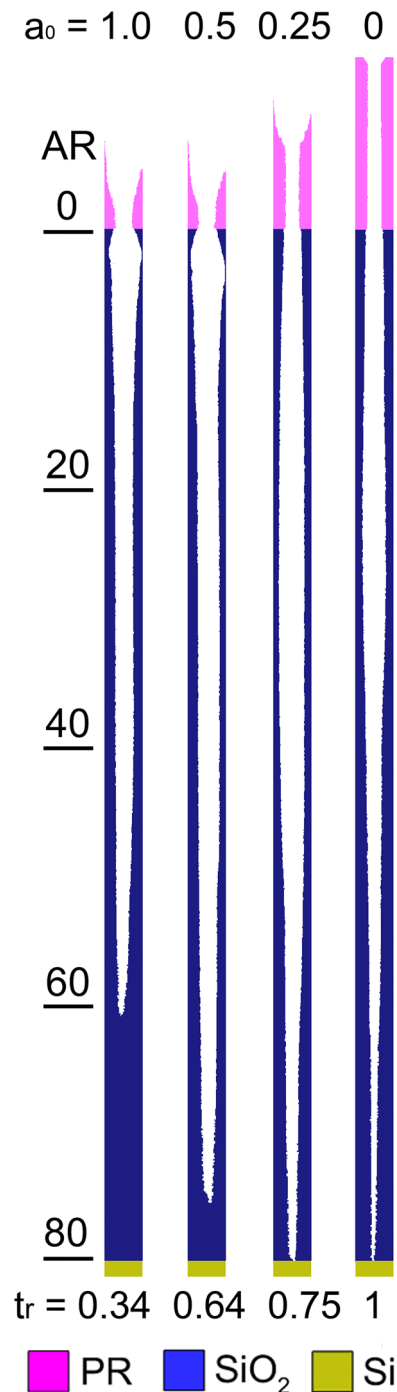


FIG. 9. Etch profiles (central slice) for features with an aspect ratio of 80 while varying the relative PR etch probabilities,  $a_0$ , from 1.0 to 0.5, 0.25, and 0 of the values specified in Table I. The relative etch time,  $t_r$ , is listed below each profile.

0% of their values in the base case, with the resulting etch profiles shown in Fig. 9. The selectivity (as indicated by the height of the PR) improves as the PR etch probability decreases while the bowing distortion decreases. Note that in the case of  $a_0 = 0.5$  and 0.25, there is significant bowing while there is no direct path for an ion reflecting from the PR facet to reach the location of bowing. The bowing for these conditions results from energetic particles having multiple reflections.

### A. 5 MHz power

A parametric study was performed of HAR etching by varying the 5 MHz power from 2.5 to 10 kW. The powers of the other two frequencies were the same as those of the base case (80/10 MHz power = 0.4/2.5 kW). The central slice of the resulting etching profiles with a 10% over-etch is shown in Fig. 10. (A 10% over-etch means that following the feature reaching the bottom Si, etching continued for an additional 10% of the time required to reach the bottom.) Over-etch is typically performed to remove the taper in the profile. The relative etch time is listed in Fig. 10. Only PR, SiO<sub>2</sub>, and Si are shown. The surface complex and the polymer have been blanked out of the figure, which is our prediction of the profiles after a cleaning process.

The fluxes of ions and hot neutrals to the etch front nearly double with increasing 5 MHz power from 2.5 to 10 kW, as shown in Fig. 11(a). This doubling is due to the increase of the initial fluxes of ions into the feature by about 50% shown in Fig. 4(b) and the narrowing of the ion angular distributions shown in Fig. 4(a), resulting in less scattering from the

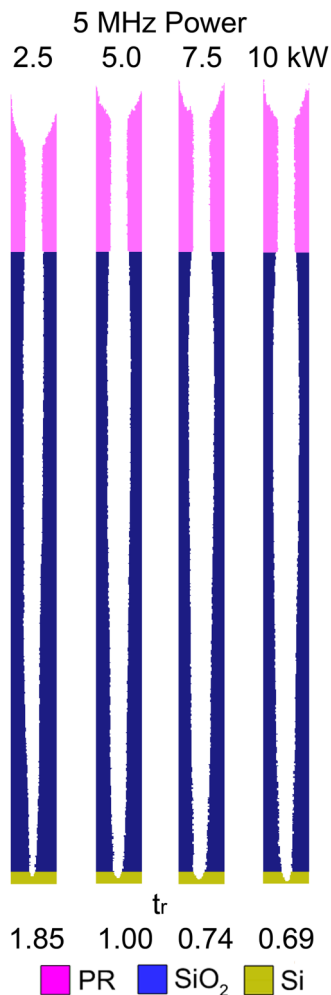


FIG. 10. Final etch profiles (central slice) with 10% over-etch of during HAR etching using fluxes and IEADs from the TF-CCP for different 5 MHz powers. Only the PR, SiO<sub>2</sub>, and Si are shown. The surface complex and polymers have been blanked out. The relative etch time,  $t_r$ , is listed below each profile. (Operating conditions: Ar/C<sub>4</sub>F<sub>8</sub>/O<sub>2</sub> = 75/15/10, 25 mTorr, 500 sccm, 80/10 MHz power = 0.4/2.5 kW, 5 MHz power: 2.5–10 kW.)

sidewalls. The power delivered by ions and hot neutrals to the etch front increases by nearly a factor of 3 with increasing 5 MHz power, as shown in Figs. 11(b) and 11(c). This increase results from both the increase in fluxes of energetic species to the etch front and an increase of their average energies by about 55%. The fractional decrease in the power delivered to the etch front by ions and hot neutrals with increasing AR is almost the same for all 5 MHz powers. These trends indicate that the transport of ions and hot neutrals into the feature is most sensitive to the aspect ratio.

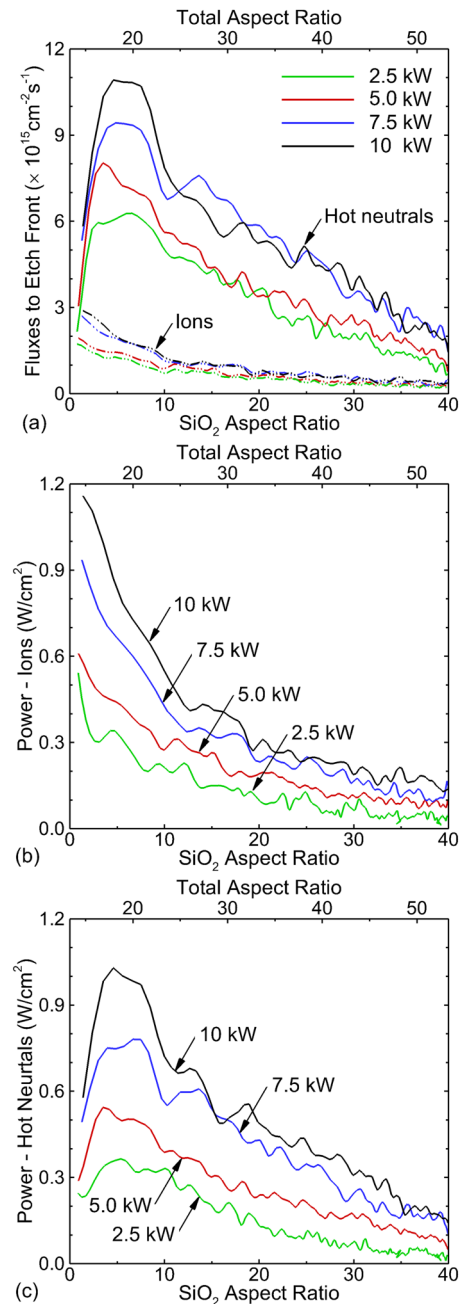


FIG. 11. Fluxes and powers to the etch front as a function of aspect ratio and power. (a) Fluxes of ions and hot neutrals to the etch front and power delivered to the etch front by (b) ions and (c) hot neutrals as a function of the aspect ratio for different 5 MHz powers. (Operating conditions: Ar/C<sub>4</sub>F<sub>8</sub>/O<sub>2</sub> = 75/15/10, 25 mTorr, 500 sccm, 80/10 MHz power = 0.4/2.5 kW, 5 MHz power: 2.5–10 kW.)

The average etch rate, selectivity, and the CDs as a function of 5 MHz power are shown in Fig. 12. The average etch rate was obtained by dividing the thickness of SiO<sub>2</sub> by the time for the etch front to reach the stopping layer and was normalized to 1 for the base case. The top CD was measured at the top of the oxide adjacent to the PR, the bottom CD was measured at the bottom of the oxide adjacent to the stopping layer, and the bowing CD was measured at the height where the diameter of the via is largest.

The efficiency of etching (rate/power) decreases when increasing the 5 MHz power. For an increase in power of a factor of 4, the etch rate increases by only a factor of 2.7. The diminishing efficiency is partly due to the increase in power by a factor of 4 producing an increase in ion flux of only 50% and an increase in average ion energy of 55%, with a fraction of the power contributing to the production of other nonreactive species. With reaction probabilities scaling with  $\epsilon^{1/2}$ , there is also a diminishing return on increasing reaction probability by increasing ion energy when the ion energy is already significantly above the threshold, as is the case here.

With the flux of thermal neutrals being conduction limited to the bottom of the feature and not significantly increasing with 5 MHz power, the etching is neutral-starved at the higher powers. Polymerizing neutrals for chemical sputtering are largely delivered by slowing hot

neutrals. Some etch rate is recouped by a moderate narrowing of the IEAD with increasing power, which enables a larger fraction of incident ions to reach the etch front without scattering from the sidewalls.

The top, bowing, and bottom CDs of the features all increase when varying 5 MHz power. According to the final profiles having the 10% over-etch shown in Fig. 10 and the measurements of CDs shown in Fig. 12(b), the top CDs are approximately 160 nm, which is about 40 nm larger than the original mask opening diameter of 120 nm. The bowing CD increases from 162 to 204 nm with increasing power, which is mainly due to the larger increase of ion flux compared with the polymerizing radical flux which protects the sidewalls. More ions are diffusively scattered or reflected from sidewalls relative to the lower rate of sidewall passivation, which results in an enhanced lateral etching of sidewalls and bowing in the upper portion of the feature. The bottom CD is sensitive to the over-etch time which determines the degree of clearing of the corners. The bottom CDs are smaller than the original mask opening due to the relatively short 10% over-etch time. For tapered etch fronts, a short over-etch time results in an incomplete corner clearing and smaller bottom CDs (50–100 nm). For these conditions, longer etch times will begin to broaden the top of the feature.

## B. (CF<sub>x</sub> + C<sub>x</sub>F<sub>y</sub>)/ion flux ratio

The transport of energetic species (hot neutrals and ions) and polymerizing radicals (CF<sub>x</sub> and C<sub>x</sub>F<sub>y</sub>) into HAR features significantly varies with increasing AR, while these two groups of species play different roles in the etching of SiO<sub>2</sub>. The CF<sub>x</sub> and C<sub>x</sub>F<sub>y</sub> radicals contribute to passivation and polymer deposition, while energetic hot neutrals and ions produce chemical and physical sputtering of the surface complex and oxide. The relative fluxes of the energetic species and fluorocarbon radicals are linked through the properties of the plasma which are in turn functions of power, pressure, flow rates, mole fractions, frequencies, and pulse waveforms. However, artificially adjusting their relative fluxes does provide an insight to the etching process. In this regard, the magnitude of the flux of all positive ions, I<sup>+</sup>, was varied while keeping the shape of the IEADs and the incident neutral fluxes constant. In doing so, the (CF<sub>x</sub> + C<sub>x</sub>F<sub>y</sub>)/I<sup>+</sup> flux ratio was varied from 5 to 40 where for the base case, the ratio is 30. The central slices of the resulting profiles with the 10% over-etch are shown in Fig. 13. The average etch rate, selectivity, and CDs are shown in Fig. 14.

As the (CF<sub>x</sub> + C<sub>x</sub>F<sub>y</sub>)/I<sup>+</sup> flux ratio increases from 5 to 40, the average etch rate and the selectivity both decrease—the flux of energetic species and power delivered to the etch front by those energetic species both decrease. The time required to etch through the oxide increases by 10 times as the (CF<sub>x</sub> + C<sub>x</sub>F<sub>y</sub>)/I<sup>+</sup> flux ratio increases from 5 to 40, resulting in an increased erosion of PR from 372 to 510 nm and a decreased SiO<sub>2</sub>/PR selectivity from 12.9 to 9.4. The strong dependence of the etch rate on the (CF<sub>x</sub> + C<sub>x</sub>F<sub>y</sub>)/I<sup>+</sup> flux ratio is mainly due to the ion-driven etching process for oxide. Increasing the flux of ions results in a higher etch rate, but

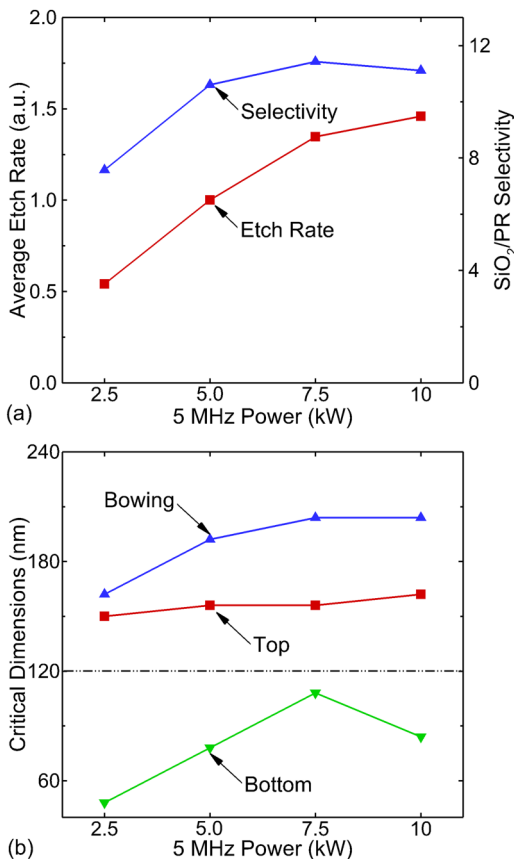


Fig. 12. Etch rates and critical dimensions for different 5 MHz powers. (a) Normalized average etch rate and SiO<sub>2</sub>/PR selectivity and (b) top, bowing, and bottom critical dimensions with 10% over-etch during HAR etching for different 5 MHz powers. The diameter of the initial mask opening is 120 nm.

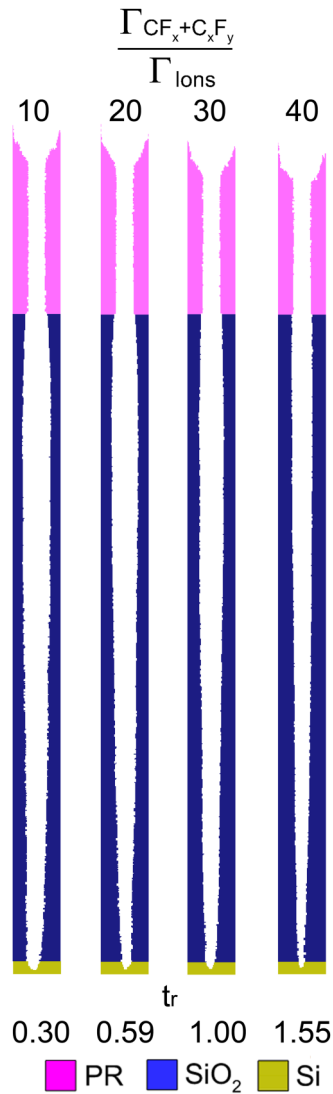


FIG. 13. Final etch profiles (central slice) with 10% over-etch of during HAR etching for different  $(CF_x + C_xF_y)/ion$  flux ratios from 5 to 40. Only PR, SiO<sub>2</sub>, and Si are shown, with the complex and polymers being blanked out. The  $(CF_x + C_xF_y)/ion$  flux ratio in the base case is 30. The fluxes of ions were varied, while the fluxes of CF<sub>x</sub> and C<sub>x</sub>F<sub>y</sub> remained constant. The same IEADs from the base case were used in all cases. The relative etch time,  $t_r$ , is listed below each feature.

also leads to more pattern degradation by increasing the top and bowing CDs, as shown in Fig. 14(b). As the  $(CF_x + C_xF_y)/I^+$  flux ratio decreases by increasing the ion flux, the lateral etching by hot neutrals and ions increases, resulting in an increase in the top CD from 156 to 168 nm and an increase in the bowing CD from 162 to 210 nm.

### C. Fractional CF<sub>x</sub><sup>+</sup> and C<sub>x</sub>F<sub>y</sub><sup>+</sup>

The CF<sub>x</sub><sup>+</sup> and C<sub>x</sub>F<sub>y</sub><sup>+</sup> ions play multiple roles in the etching of oxide. These energetic ions and their hot neutral partners can remove oxide directly through physical sputtering or remove the complex through chemically enhanced sputtering. After losing energy through several collisions with the sidewalls and the etch front, these energetic species become thermal CF<sub>x</sub> and C<sub>x</sub>F<sub>y</sub> radicals, which can passivate

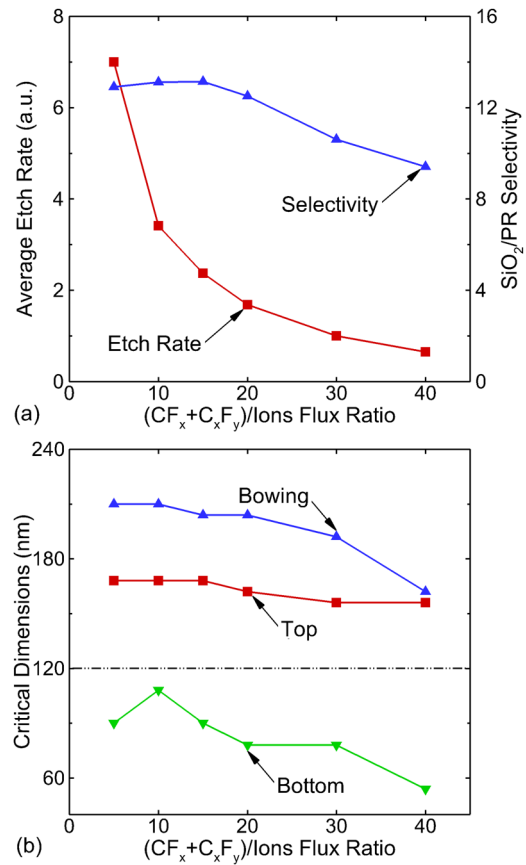


FIG. 14. Etch rates and critical dimensions for different radical to ion ratios. (a) Normalized average etch rate and SiO<sub>2</sub>/PR selectivity and (b) top, bowing, and bottom critical dimensions with 10% over-etch for different  $(CF_x + C_xF_y)/ion$  flux ratios. The  $(CF_x + C_xF_y)/ion$  flux ratio in the base case is 30. The fluxes of ions were varied, while the fluxes of CF<sub>x</sub> and C<sub>x</sub>F<sub>y</sub> remained constant. The same IEADs from the base case were used for all cases. The diameter of the initial mask opening is 120 nm.

the oxide surface or deposit as a polymer. In the base case, the majority of the CF<sub>x</sub> and C<sub>x</sub>F<sub>y</sub> radicals at low AR (<5), shown in Fig. 6(a), originates from the thermal neutrals incident into the feature from the plasma. As the AR increases to greater than 10, the neutralized and thermalized CF<sub>x</sub><sup>+</sup> and C<sub>x</sub>F<sub>y</sub><sup>+</sup> ions become the main source (>95%) of radicals reaching the etch front. To investigate these processes, the fluxes of CF<sub>x</sub><sup>+</sup> and C<sub>x</sub>F<sub>y</sub><sup>+</sup> were varied, while the total ion flux was maintained constant by decreasing the flux of Ar<sup>+</sup> whose neutral partner is chemically nonreactive. In this manner, the fraction of CF<sub>x</sub><sup>+</sup> and C<sub>x</sub>F<sub>y</sub><sup>+</sup> fluxes,  $(CF_x^+ + C_xF_y^+)/I^+$ , was varied from 15% to 60%. (For the base case, the fraction of CF<sub>x</sub><sup>+</sup> and C<sub>x</sub>F<sub>y</sub><sup>+</sup> ions is 30%.) The final etch profiles with the 10% over-etch are shown in Fig. 15. The average etch rate, selectivity, and CDs are shown in Fig. 16.

As the majority of the CF<sub>x</sub> and C<sub>x</sub>F<sub>y</sub> radicals reaching deep into the feature (AR > 10) originates from CF<sub>x</sub><sup>+</sup> and C<sub>x</sub>F<sub>y</sub><sup>+</sup>, the flux of CF<sub>x</sub> and C<sub>x</sub>F<sub>y</sub> to the etch front at a high AR increases by approximately three times when increasing fractional CF<sub>x</sub><sup>+</sup> and C<sub>x</sub>F<sub>y</sub><sup>+</sup>. This increase in fluorocarbon radicals to the etch front results in more surface passivation and polymer deposition which requires additional ions to remove the oxide. The neutral and thermalized partners of other ions

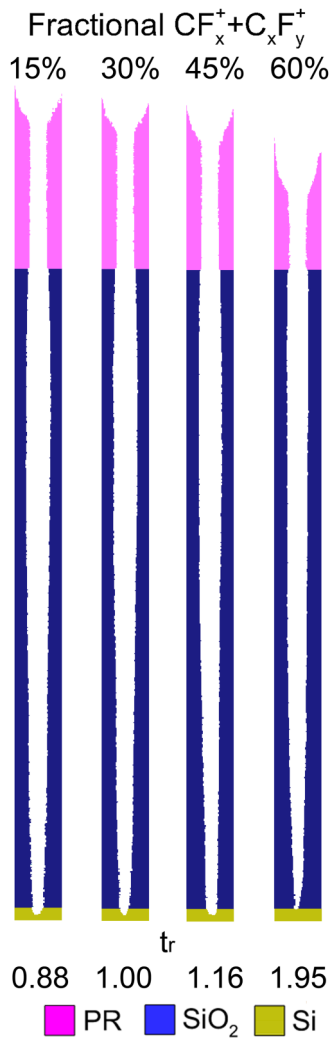


Fig. 15. Final etching profiles (central slice) with 10% over-etch for HAR etching for different fractional  $CF_x^+$  and  $C_xF_y^+$ . Only the PR, SiO<sub>2</sub>, and Si are shown, with the complex and polymers being blanked out. The fractional  $CF_x^+$  and  $C_xF_y^+$  in the base case is 15%. The fluxes of  $CF_x^+$  and  $C_xF_y^+$  ions were varied, while the total ion flux was maintained constant by decreasing the flux of Ar<sup>+</sup>. The same IEADs from the base case were used for all cases. The relative etch time,  $t_r$ , is listed below each feature.

are nonreactive species and diffuse out of the feature with no surface reactions (only scattering at the surface). There is little surface passivation or polymer deposition resulting from those thermalized species. Thus, the etch rate of oxide decreases by about 30% when increasing the fraction of  $CF_x^+$  and  $C_xF_y^+$ , as shown in Fig. 16(a). The ratio of material removed by chemical sputtering versus physical sputtering increases with increasing fractions of  $CF_x^+$  and  $C_xF_y^+$ , from 1.1 to 3.5. The etch rate of PR is almost invariant with the fraction of  $CF_x^+$  and  $C_xF_y^+$  as, in this model, all of the ions have the same energy and angular dependent probabilities for physical sputtering of the PR. Ions reflecting from the top of the PR as hot neutrals will, in most cases, scatter back into the plasma, and not directly revisit the PR. So, the SiO<sub>2</sub>/PR selectivity also decreases by about 50% with the increasing fraction of  $CF_x^+$  and  $C_xF_y^+$ . We expect that there will be a mass dependence on PR sputtering rates by different ions.

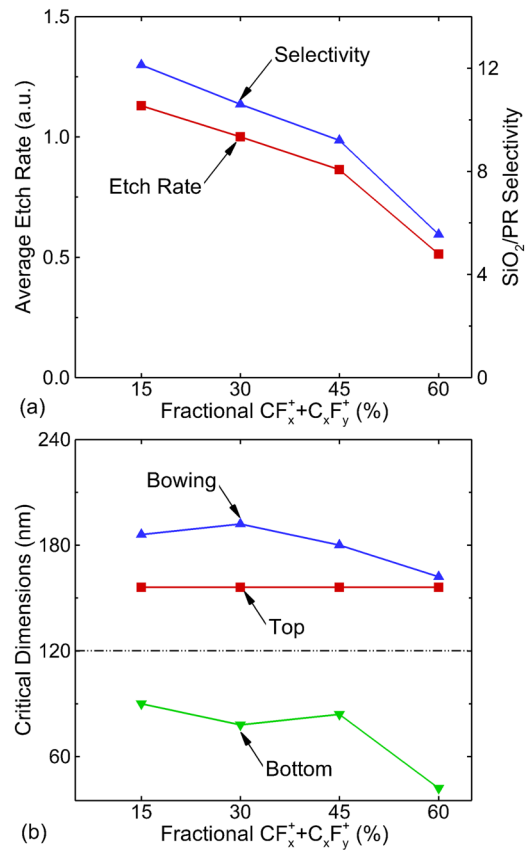


Fig. 16. Etch rates and critical dimensions as a function of fluorocarbon ion flux. (a) Normalized average etch rate and SiO<sub>2</sub>/PR selectivity, and (b) top, bowing, and bottom critical dimensions with 10% over-etch during HAR etching for different fractional  $CF_x^+$  and  $C_xF_y^+$ . The fractional  $CF_x^+$  and  $C_xF_y^+$  in the base case is 15%. The fluxes of  $CF_x^+$  and  $C_xF_y^+$  ions were varied, while the total ion flux was maintained constant by decreasing adjusting the flux of Ar<sup>+</sup>. The same IEADs from the base case were used for all cases. The diameter of the initial mask opening is 120 nm.

However, since all ions are heavy compared with the components of the hydrocarbon polymer of the PR, that mass dependence of sputtering will not be large.

An effect that has not been included in the reaction mechanism is dissociation of molecular ions and hot neutrals when striking the surface. There are large fluxes of fluorocarbon ions whose neutral counterparts are nonreactive, such as  $C_2F_4^+$ . However,  $C_xF_y^+$  ions of many hundreds of eV to a few keV, as in this study, will likely fragment when striking the surface.<sup>51</sup> This fragmentation will then increase the flux of more reactive and smaller neutral species,  $CF_x$ , which are more likely to polymerize and form surface complexes.

The top, bowing, and bottom CDs shown in Fig. 16(b) vary only slightly with increasing fractional  $CF_x^+$  and  $C_xF_y^+$ , being maintained at about 156, 180, and 84 nm, respectively. The increased fluxes of  $CF_x$  and  $C_xF_y$  radicals deep into the feature with increasing fractional  $CF_x^+$  and  $C_xF_y^+$  provide protection to the sidewalls from lateral etching, which is offset by the longer etch time resulting from the decrease in the rate. The end result is only small variations in the CDs for different fractional  $CF_x^+$  and  $C_xF_y^+$ . The small bottom CD of 42 nm with fractional  $CF_x^+$

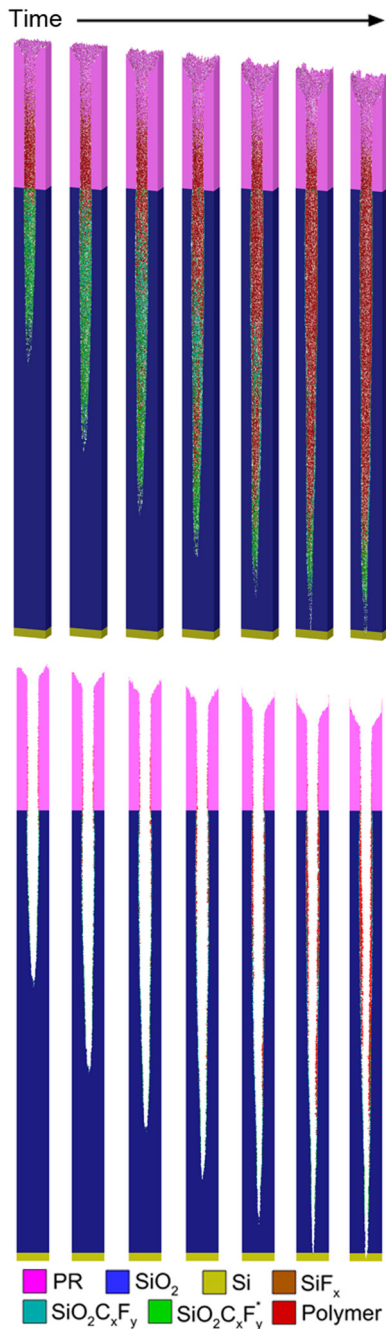


FIG. 17. Etch profiles during HAR etching with charging. Section view (top) and central slice (bottom). The same fluxes and IEADs from the TF-CCP were used as in the noncharging cases shown in Fig. 5. The time intervals between the adjacent profiles are the same as in Fig. 5. (Operating conditions: Ar/C<sub>4</sub>F<sub>8</sub>/O<sub>2</sub> = 75/15/10, 25 mTorr, 500 sccm, 80/10/5 MHz power = 0.4/2.5/5 kW.)

and C<sub>x</sub>F<sub>y</sub><sup>+</sup> of 60% is mainly due to there being more polymerizing species from thermalized ion partners and a longer over-etch time required for clearing the corner.

#### D. Charging of features

Charging of the surfaces on the top and inside of the feature occurs in dielectric etching or in conductor etching using polymerizing gas mixtures. The same HAR geometry,

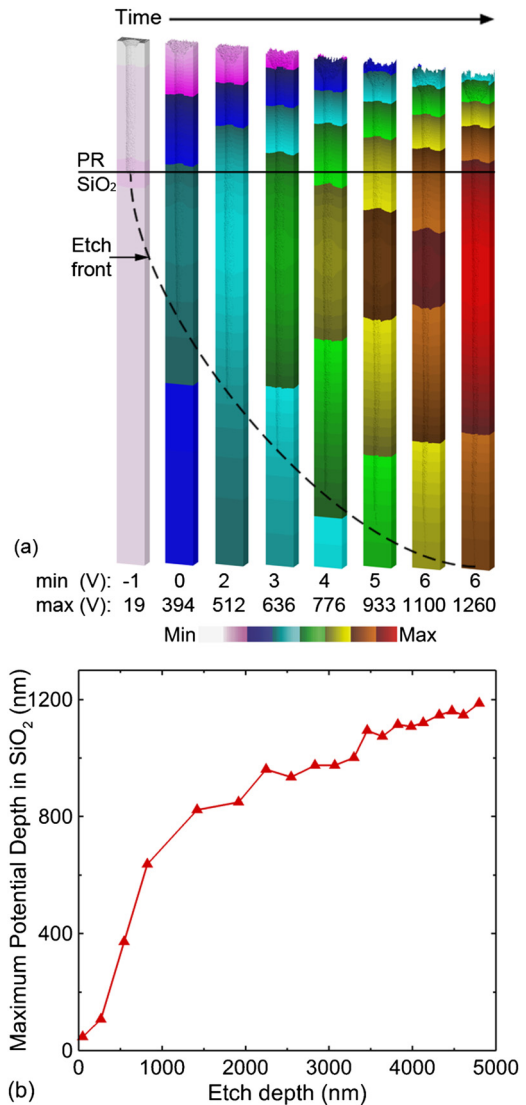


FIG. 18. Electrical potential due to charging. (a) Time evolution of the electric potential (section view) in the feature and (b) correlation between the depth of maximum potential in SiO<sub>2</sub> and the etch depth as the HAR etching proceeds. The first frame in (a) is at the very beginning of the etching, while the other seven frames in (a) are sampled from at the same time as in Fig. 17. The location of the etch front is shown in (a). The same fluxes and IEADs from the TF-CCP were used as in the noncharging cases.

IEADs, and fluxes as in the base case were used in simulations when including charging effects. The time evolution of the etch profiles and the electric potentials in and around the features are shown in Figs. 17 and 18(a). The profiles in Fig. 17 are shown at the same time intervals as those for the noncharging base case (Fig. 5) so that side-by-side comparisons can be made. The first frame in Fig. 18(a) is at the very beginning of etching where the maximum of the positive potential is at the bottom of the feature, while the other seven frames in Fig. 18(a) are sampled at the same rate as that of the frames in Fig. 17.

The top surface of the PR is almost charge neutral or slightly negatively charged. Even though the electron flux has a Lambertian angular distribution, while the positive ions have a narrow angular distribution about the normal, the

net conduction current to a flat nonconducting surface should be zero averaged over the rf period. (The flux of negative ions is essentially zero compared with other charged particle fluxes.) However, this disparity in angular distributions of electrons and ions results in electrons dominantly initially charging the top surface and surfaces having a small AR, while the ions can reach deep into the features.<sup>52</sup> The end result is that for a small AR, the feature initially negatively charges on inside surfaces near the top and positively charges near the bottom of the feature. This charging is reflected by the positive plasma potential that appears on the bottom of the feature at the beginning of etching, as shown in Fig. 18(a). The positive charging slows ions as they approach the bottom of the feature. If this situation persists, the bottom of the feature would charge to a positive potential essentially equal to the energy of the incident ions which would deflect ions back out of the feature (or into walls) to prevent further charging. Etching would then cease. In the steady state, the positive potential attracts electrons into the feature to neutralize the continuous positive charge delivered by the anisotropic ions. The end result is a steady-state positive charge and potential distribution in the feature.

We note that there are several other strategies to control charging of features that rely on pulsed plasmas.<sup>22,23</sup> In this approach, the source power is pulsed producing an active glow discharge, followed by an afterglow in which electrons rapidly attach to form a positive ion–negative ion plasma. Application of a bias during the afterglow then accelerates negative ions into the feature to neutralize excess positive charge.

The net positive charge in the feature produces both vertical and lateral electric fields which can perturb the velocities and deviate the trajectories of the subsequent positive incident ions. The result is a decrease in the etch rate and an increased time to etch through the feature by about 30% compared with the noncharging case. This mild effect of charging is in part a consequence of the high aspect ratio. In high volume manufacturing, the etching of HAR vias in silicon oxide having an AR of 40–50 takes as long as 40–50 min. The predicted etch times here are 36 min for the base case without charging (Fig. 5) and 48 min for the base case with charging (Fig. 17), which are in reasonable agreement with experiments.

At the beginning of etching when the AR is small, the position of the maximum electric potential is near the etch front where most of the ions first hit the surface and deposit charge. As the etching proceeds and the AR increases, the position of the maximum potential initially moves downward before becoming nearly static in the upper portion of the feature, as shown in Fig. 18(b). By an AR of about 10, the majority of ions will have collided with the sidewalls where they deposit charge, then proceeding as hot neutrals which are not affected by the electric fields. When the etch front reaches the bottom stop layer, the maximum electric potential higher in the feature (AR ≈ 10) is 1100 V, which is about 60% of the average energy of incident ions. Had this maximum been at the bottom of the feature, the ion energy incident onto the etch front would have decreased by about 60%. However, with the maximum in potential being higher

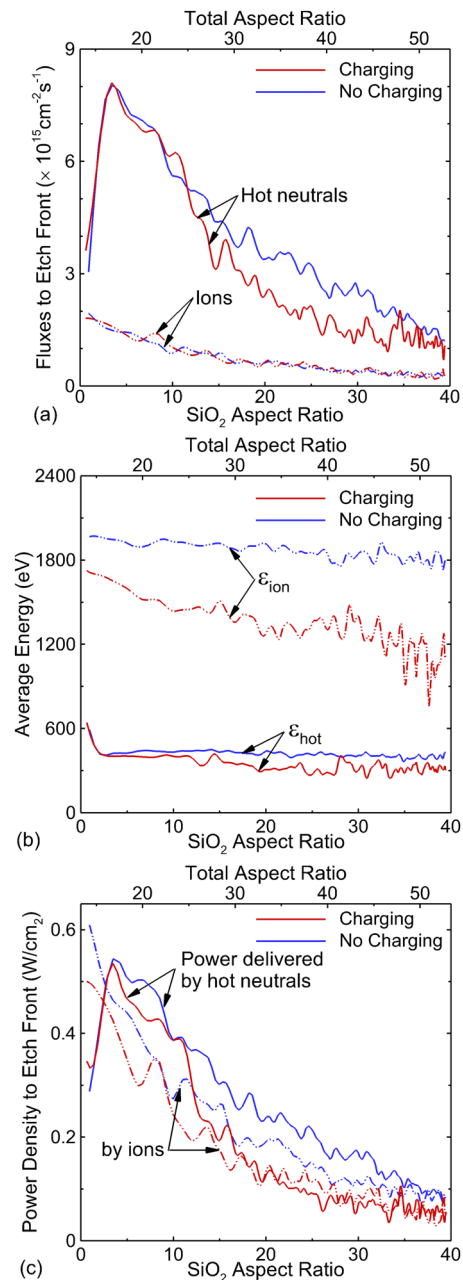


Fig. 19. Fluxes and powers to the etch front with and without charging. (a) Fluxes and (b) average energy of ions and hot neutrals to the etch front, and (c) power delivered to the etch front by ions and hot neutrals as a function of the aspect ratio for the base case.

in the feature, ions are decelerated when approaching the maximum in potential and accelerated when passing the maximum, with less net change in energy.

In previous experimental and numerical investigations of oxide plasma etching using fluorocarbon gas mixtures, the maximum electric potentials in the feature were 200 V at AR = 20 (Ref. 1), 300 V at AR = 10 (Ref. 53), and 150 V at AR = 15 (Ref. 54). In this study, the maximum potentials at ARs of 10–20 are 200–400 V, which are commensurate with these prior results. Our higher in-feature potentials result in large part from the higher ion energies that are required for HAR etching. There is a secondary effect of transport of

electron thermal flux from the plasma into the feature. There is some continual neutralization of positive charge on the sidewalls of features by electron flux that is pulled into the feature by the electric fields produced by the positive in-feature potential. As the AR increases, the available electron flux from the plasma to neutralize positive charge decreases.

Comparisons of the fluxes and average energies of ions and hot neutrals, and power delivered to the etch front as a function of AR with and without charging are shown in Fig. 19. The ion and hot neutral fluxes are nearly independent of charging. With the maximum of the electric potential appearing in the upper portion of the feature, the sequence of deceleration of ions at low ARs and then acceleration at high ARs results in only a nominal reduction of ion energy for low to moderate AR. As the AR increases to above 10, there is a gradual decrease in ion energy to the feature relative to the base case without charging. This decrease results in part from there being an increase in the positive potential that affects ions having progressively narrower angular distributions. For an AR of 40, charging produces a decrease of the average energy of ions to the etch front from 1940 to 1050 eV.

The hot neutrals originate from neutralized ions that undergo grazing incidence and specular reflection at the sidewalls. The majority of the energy is maintained and the reflected angles are shallow enough to direct the hot neutrals to the etch front, with the hot neutrals being unaffected by the electric field in the feature. As a result, the

fluxes of hot neutrals to the etch front are similar with and without charging, as shown in Fig. 19(a). The average energy of the hot neutrals decreases by about 50–150 eV with charging, as shown in Fig. 19(b). This decrease results from the original ions being decelerated by the electric field at low ARs before being neutralized. If ions are converted to hot neutrals before being reaccelerated when passing below the maximum in potential, the hot neutrals proceed to the etch front with a lower energy. The power delivered to the etch front by hot neutrals with charging is smaller than without charging by about 15%, as shown in Fig. 19(c). This lower power flux is mainly due to the lower average energy of hot neutrals. The end result is a decrease in the etch rate with charging.

The effect of charging is sensitive to the 5 MHz power due to the incident ions having different IEADs. When increasing 5 MHz power from 2.5 to 10 kW, the average energy of ions reaching the bottom of the feature (AR = 40) increases from 1400 to 2460 eV without charging, while increasing from 475 to 1760 eV with charging, as shown in Fig. 20(a). The fractional decrease in ion energy is more severe for lower power. The difference in ion energy with and without charging ( $\Delta E = E_{chg} - E_0$ ) decreases from 925 eV at 2.5 kW to 700 eV at 10 kW, which corresponds to fraction decrease,  $\Delta E/E_0$ , from about 66% to 28%, as shown in Fig. 20(b). In fact, the decrease in ion energy produces an etch stop at 2.5 kW before reaching AR = 40. (The average ion energy in Fig. 20(a) for 2.5 kW is an extrapolation from smaller AR.) The charging of the sidewalls scales with the ion flux which is a weak function of 5 MHz power, whereas the energy of the ions scales as 5 MHz power. The end result is that the increase in plasma potential lags behind the increase in ion energy. There is also a secondary effect that the etch rate is higher at higher power. A higher etch rate translates to a shorter etch time and a smaller fluence of positive ions into the feature. This smaller fluence of positive ions results in less charge deposition and a smaller positive potential.

All of the materials in these features are nonconductors, and so the mobility of charge on or through these materials is expected to be negligible. For example, the electron mobility through fluorocarbon polymer (polytetrafluoroethylene) is  $10^{-11}$  cm<sup>2</sup>/V s.<sup>55</sup> As a result, the charge on the sidewalls in these simulations was static. That is, the charge did not move on or along the surface. The MCFPM has the ability to allow transport of charge through solid materials and include that change of charge in a solution of Poisson's equation for the electric potential. This capability is needed in simulations with conducting material. To test our assumption that electron charge is static on surfaces, simulations were conducted where electrons on polymer were given a nonzero mobility, varied with values as large as  $10^{-3}$  cm<sup>2</sup>/V-s. The result was that the charge did migrate through the polymer, which resulted in a net reduction of the total charge in the feature due to a recombination between positive and negative charges. However, the mobilities for which these effects were significant were many orders of magnitude larger than what might be expected for fluorine containing polymers. So, our assumption of immobile electron charge on surfaces is likely accurate.

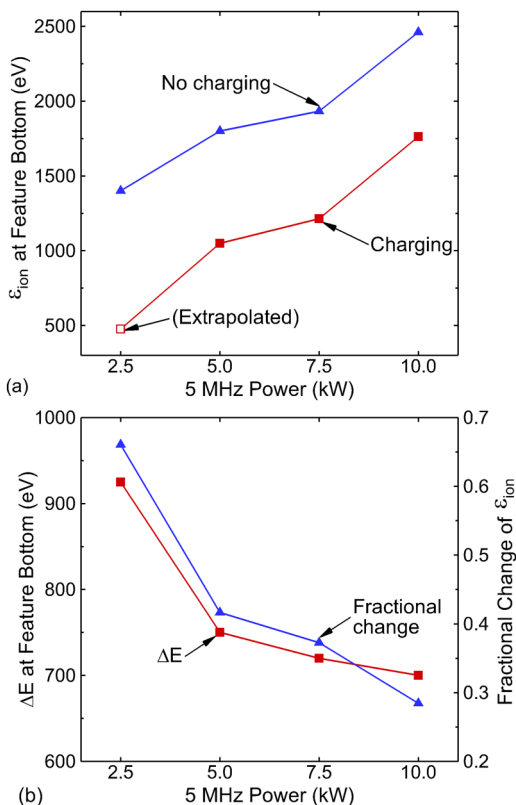


FIG. 20. Properties of ions striking the bottom of the feature with and without charging. (a) The average energy of ions and (b) the absolute and fractional difference between the average energy of ions reaching the feature bottom for cases with and without charging.

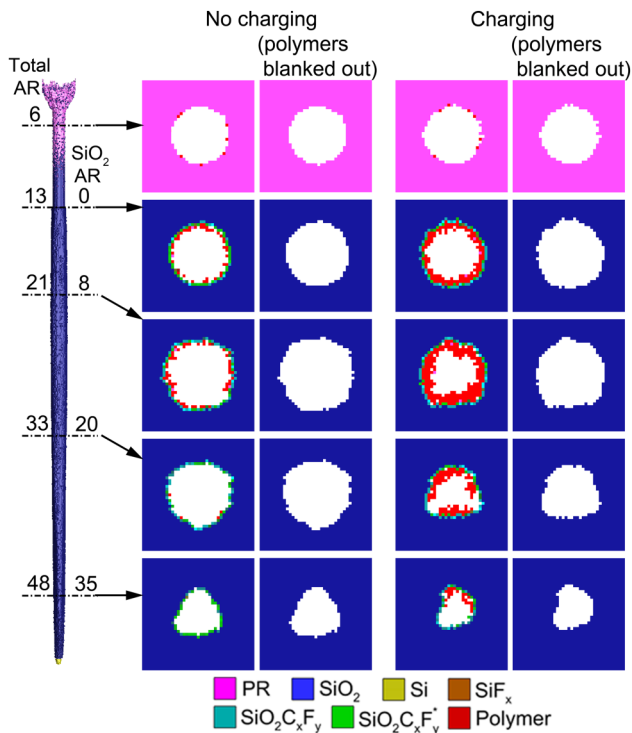


Fig. 21. Horizontal slices through the final etching profiles with 10% over-etch for the base case without and with charging. The left column shows profiles with the surface complex and polymers. The right column shows only the PR, SiO<sub>2</sub>, and Si, with complex and polymers being blanked out. Stochastic processes produce noncircular profiles deep in the feature. (Operating conditions: Ar/C<sub>4</sub>F<sub>8</sub>/O<sub>2</sub> = 75/15/10, 25 mTorr, 500 sccm, 80/10/5 MHz power = 0.4/2.5/5 kW.)

### E. Feature distortion

Feature distortion refers to producing an etch profile that does not replicate the intended pattern defined by the photolithography. Feature distortion includes line (or contact) etch roughness, twisting, and producing noncircular vias.<sup>3,9,56</sup> The latter feature distortion is shown in Fig. 21, where horizontal sections of the feature are shown (with and without charging) at different heights in the feature. A small amount of roughness occurs on the walls of the PR due to the randomness and statistical nature of the grazing angle sputtering of the mask. This roughness then results in a more diffusive scattering of grazing angle ions, which then leads to bowing deeper in the feature. However, without charging, as deep as AR = 20, the cross section of the final feature is basically circular, with some statistical roughness. Deeper into the feature (higher AR), the cross section of the feature deviates from a circular profile. This deviation occurs to some extent at all heights, resulting from the initially tapered etch front rarely being circular. However, an effective over-etch occurs at all heights above the bottom of the feature. (That is, heights above the etch front continue to experience sidewall scattering.) This effective over-etch is the time between achieving the desired CD at a given height to the end of etching. The over-etch tends to round previously noncircular features and removes the anomalies caused by the tapered etch front. The end result is that noncircular cross sections tend to occur in the lower portion of the feature that experiences a less

effective over-etch. The rounding of the feature by over-etch is less effective with charging.

The thickness of the polymer deposited on the sidewalls varies as a function of AR and is typically larger when including charging. Predicted polymer thickness ranges from 0 to about 20 nm with a maximum thickness occurring at AR = 8. Experimentally, the sidewall polymer thickness is a function of many operational parameters (e.g., bias power, pressure, gas mixture, wafer temperature) and has been measured to be 20–100 nm (Ref. 1) and 5–20 nm (Ref. 57) during HAR etching for ARs of 10–20 using fluorocarbon gas mixtures.

The origin of the noncircular cross sections is largely simply statistics. The area of the mask opening in HAR etching has decreased more rapidly than the reactant flux incident onto the mask has increased. The end result is that the number of particles/second entering the feature has decreased to the point that the type (e.g., radical versus ion), energy, and angle of reactants is subject to statistical noise. This statistical noise produces statistically noisy reactions with the surface, from polymer deposition to chemical sputtering. As the etch depth and AR increases, the fluxes of reactants reaching the etch front decrease due to conduction limits, resulting in more statistical sampling of these fluxes. The diameter of the hole also decreases with increasing AR due to tapering. Holes with smaller diameters are more sensitive to small surface imperfections, which then produce shadowing deeper into the feature. The end result is a noncircular cross section of the feature. Over-etch improves upon those statistics by simply having more particles interact with the feature at that height.

Charging aggravates feature distortion by introducing more randomness and more persistence of randomness to the process. For example, horizontal slices at different heights of the final profile with a 10% over-etch are shown with charging in Fig. 21 for the base case. With charging, feature distortion begins at ARs as low as 10. This additional distortion results from the randomness of charge deposition on the sidewalls, and particularly charge that is trapped in a polymer that is persistent. The polymer films on the sidewall with charging are thicker and less uniform than without charging, resulting in a deeper trapped charge. The resulting electric fields then perturb the trajectories of ions, perturbations that are then imprinted into the specular hot neutrals. Since the charging of the feature is not azimuthally nor axially uniform, both of which have some randomness, feature distortion is worse with charging.

### VI. CONCLUDING REMARKS

The etching of HAR features in SiO<sub>2</sub> with aspect ratios up to 80 was investigated using integrated reactor and feature scale modeling. A triple-frequency CCP reactor sustained in Ar/C<sub>4</sub>F<sub>8</sub>/O<sub>2</sub> mixtures was used as a source of radicals and ions and modeled in two-dimensions. The IEADs and fluxes of ions and neutrals to the wafer obtained from the reactor scale modeling were used in the three-dimensional MCFPM to predict feature evolution. In the TF-CCP reactor, the dominant fluxes of radicals to the wafer surface are CF<sub>x</sub>, F, and O, which are mainly produced through electron impact dissociation of feedstock C<sub>4</sub>F<sub>8</sub> and O<sub>2</sub> gases. Fluxes of ions are lower

than those of radicals by 1–2 orders of magnitude. The incident ions have energies of up to several keV and incident angles of less than 4°.

During HAR etching, bowing occurs in the upper portion of the feature due to diffusive scattering of ions at the sidewalls of the PR and erosion of PR with increasing facet area for ion reflection which produce hot neutrals into the feature with broadened angular distributions. At low ARs (<5), abundant fluxes of CF<sub>x</sub> and C<sub>x</sub>F<sub>y</sub> radicals passivate the oxide surface to form complexes which are then removed by energetic species (hot neutrals and ions) through chemically enhanced sputtering with the formation of gas phase SiF<sub>x</sub>, CO<sub>x</sub>, and COF. As the AR increases, conductance limits on the initially isotropic thermal radicals reduce their fluxes reaching deeply into the feature. For a sufficiently large AR, the neutral radicals reaching the bottom of the feature originate from neutralized ions that can overcome conductance limits by virtue of their initially anisotropic trajectories. The dominant oxide removal process transitions from chemical to physical sputtering as the fluxes of energetic species to the etch front surpass those of radicals.

ARDE, decreasing etch rate with increasing etch depth or AR, was observed in all cases. ARDE results from both lack of neutral radicals by conductance limits and a decrease in the power delivered to the etch front as AR increases. Erosion of PR, being more akin to blanket etching, does not depend on either the height of the PR or the AR of the feature being etching. With ARDE decreasing the SiO<sub>2</sub> etch rate, the PR selectivity worsens with increasing AR. In this example, in etching to an AR of 80, the PR was almost fully eroded. This scaling would suggest that increasing PR height with increasing AR to be etched would preserve CD. However, there is a limit to this scaling as the PR itself has an AR adding to the effective AR that incident species experience arriving at SiO<sub>2</sub>. This increase in AR affects ion and neutral transport in the same way that AR affects transport in the feature. Increasing the height of the PR increases ARDE by adding to conductance limits and reducing ion and hot neutral energies reaching SiO<sub>2</sub>.

Parametric studies for the etch process were performed by varying the 5 MHz source power, (CF<sub>x</sub> + C<sub>x</sub>F<sub>y</sub>)/ion flux ratio and fractional of the ion flux consisting of CF<sub>x</sub><sup>+</sup> and C<sub>x</sub>F<sub>y</sub><sup>+</sup>. The etch rate of the oxide increases with increasing 5 MHz power, while the SiO<sub>2</sub>/PR selectivity remains almost invariant as the increase in fluxes of ions favors the removal of both SiO<sub>2</sub> and PR in the same ratios. Due to the coupling of the production of ions and radicals in plasmas, the fluxes were artificially adjusted to provide insights into the etching process. Decreasing the (CF<sub>x</sub> + C<sub>x</sub>F<sub>y</sub>)/ion flux ratio by increasing the flux of incident ions results in higher etch rate and selectivity, at the cost of more bowing due to polymer deposition on the sidewalls being removed by energetic species. As the majority of the CF<sub>x</sub> and C<sub>x</sub>F<sub>y</sub> radicals reaching deeply into the feature (AR > 10) originate from CF<sub>x</sub><sup>+</sup> and C<sub>x</sub>F<sub>y</sub><sup>+</sup> ions, the flux of CF<sub>x</sub> and C<sub>x</sub>F<sub>y</sub> to the etch front increases with an increasing fraction of CF<sub>x</sub><sup>+</sup> and C<sub>x</sub>F<sub>y</sub><sup>+</sup>, resulting in more surface passivation and polymer deposition which requires an additional ion flux to remove the oxide.

Thus, the etch rate of the oxide and SiO<sub>2</sub>/PR selectivity both decrease with an increasing fraction of CF<sub>x</sub><sup>+</sup> and C<sub>x</sub>F<sub>y</sub><sup>+</sup>.

When including charging, the top surface of the PR is almost charge neutral or slightly negatively charged due to balancing of the Lambertian angular distributions of electrons and the anisotropic ions on flat surfaces. Energetic positive ions can reach deeply into features and deposit positive charge, producing electric fields that decelerate and deviate the subsequent ions. The deceleration results in a reduction in etch rate due to lower power delivered by the energetic species to the etch front. At low AR, the most positively charged surface is the bottom of the feature. With increasing AR, the most positive electric potential occurs on the sidewalls where ions have their first collisions. The effect of charging becomes less significant as the bias power increases mainly due to the increased average energy of incident ions, which undergo smaller fractional energy loss when transporting to the bottom of the feature and shorter charging time producing a smaller potential buildup inside the feature.

The etching of extremely high aspect ratio features requires a more stringent control of IEADs and neutral-to-ion flux ratios. This more stringent control has motivated the development of multifrequency sources having large dynamic ranges for tuning IEADs and flux ratios with the goal of having a large process window for optimization. At a high AR, the reactive radicals CF<sub>x</sub> and C<sub>x</sub>F<sub>y</sub> reaching the etch front mainly originate from the incident ion partners CF<sub>x</sub><sup>+</sup> and C<sub>x</sub>F<sub>y</sub><sup>+</sup>. To maintain process rates and CDs at high AR, it is necessary to control both the fractional fluxes of these ions while increasing ion fluxes to both provide activation energy and radicals to the etch front. Although at a high AR, nonreactive ions such as Ar<sup>+</sup> provide activation energy to the etch front through their hot-neutral partner, these ions do not provide chemical reactivity. High AR processes thereby likely also require a larger fraction of CF<sub>x</sub><sup>+</sup> and C<sub>x</sub>F<sub>y</sub><sup>+</sup> ions whose neutral partners are reactive.

This study has focused on HAR etching of a single via in a single material, SiO<sub>2</sub>. However, many of the current etching challenges involve more complex conditions. For example, pattern dependent effects have been observed where the CD of HAR features depends on the pattern with which those features are arranged on the die (e.g., rectilinear, honeycomb). The spacings of these features in 3D-NAND memory may be as small as 50–100 nm, dimensions so small that there is no systematic change in the incident reactant fluxes. These pattern dependent processes therefore likely result from interactions between features. 3D-NAND memory applications also bring the challenge of etching alternately deposited materials (e.g., oxide-nitride-oxide stacks). To minimize the sensitivity of processes etching different materials to small changes in reactive fluxes, these processes will be more stable when the etch mechanism is based more on physical than on chemical reactions.

## ACKNOWLEDGMENTS

This work was supported by the Samsung Electronics Co. Ltd., the Department of Energy Office of Fusion Energy Science (Nos. DE-SC0001319 and DE-SC0014132), and the National Science Foundation (No. PHY-1500126).

- <sup>1</sup>N. Negishi, M. Miyake, K. Yokogawa, M. Oyama, T. Kanekiyo, and M. Izawa, *J. Vac. Sci. Technol. B* **35**, 051205 (2017).
- <sup>2</sup>T. Tandou, S. Kubo, K. Yokogawa, N. Negishi, and M. Izawa, *Precis. Eng.* **44**, 87 (2016).
- <sup>3</sup>T. Iwase, M. Matsui, K. Yokogawa, T. Arase, and M. Mori, *Jpn. J. Appl. Phys.* **55**, 06HB02 (2016).
- <sup>4</sup>B. Wu, A. Kumar, and S. Pamarthy, *J. Appl. Phys.* **108**, 051101 (2010).
- <sup>5</sup>H. W. Cheong, W. H. Lee, J. W. Kim, W. S. Kim, and K. W. Whang, *Plasma Sources Sci. Technol.* **23**, 065051 (2014).
- <sup>6</sup>M. Miyake, N. Negishi, M. Izawa, K. Yokogawa, M. Oyama, and T. Kanekiyo, *Jpn. J. Appl. Phys.* **48**, 08HE01 (2009).
- <sup>7</sup>S.-M. Kim, S. Koo, J.-T. Park, C.-M. Lim, M. Kim, C.-N. Ahn, A. Fumar-Pici, and A. C. Chen, *Proc. SPIE* **9048**, 90480A (2014).
- <sup>8</sup>K. Ishikawa, K. Karahashi, T. Ishijima, S. I. Cho, S. Elliott, D. Hausmann, D. Mocuta, A. Wilson, and K. Kinoshita, *Jpn. J. Appl. Phys.* **57**, 06JA01 (2018).
- <sup>9</sup>J. K. Kim, S. H. Lee, S. I. Cho, and G. Y. Yeom, *J. Vac. Sci. Technol. A* **33**, 021303 (2015).
- <sup>10</sup>V. Constantoudis, V.-K. M. Kuppuswamy, and E. Gogolides, *J. Micro/Nanolithogr. MEMS MOEMS* **12**, 013005 (2013).
- <sup>11</sup>C. Petti, *Proc. SPIE* **10589**, 1058904 (2018).
- <sup>12</sup>K. J. Kanarik, T. Lill, E. A. Hudson, S. Sriraman, S. Tan, J. Marks, V. Vahedi, and R. A. Gottscho, *J. Vac. Sci. Technol. A* **33**, 020802 (2015).
- <sup>13</sup>J.-K. Lee, I.-Y. Jang, S.-H. Lee, C.-K. Kim, and S. H. Moon, *J. Electrochem. Soc.* **156**, D269 (2009).
- <sup>14</sup>J.-K. Lee, I.-Y. Jang, S.-H. Lee, C.-K. Kim, and S. H. Moon, *J. Electrochem. Soc.* **157**, D142 (2010).
- <sup>15</sup>H. Toyoda, H. Morishima, R. Fukute, Y. Hori, I. Murakami, and H. Sugai, *J. Appl. Phys.* **95**, 5172 (2004).
- <sup>16</sup>T. Shibano, N. Fujiwara, M. Hirayama, H. Nagata, and K. Demizu, *Appl. Phys. Lett.* **63**, 2336 (1993).
- <sup>17</sup>N. Kuboi, T. Tatsumi, S. Kobayashi, T. Kinoshita, J. Komachi, M. Fukasawa, and H. Ansai, *Appl. Phys. Express* **5**, 126201 (2012).
- <sup>18</sup>N. Kuboi, T. Tatsumi, H. Minari, M. Fukasawa, Y. Zaizen, J. Komachi, and T. Kawamura, *J. Vac. Sci. Technol. A* **35**, 061306 (2017).
- <sup>19</sup>H. Ito, T. Kuwahara, Y. Higuchi, N. Ozawa, S. Samukawa, and M. Kubo, *Jpn. J. Appl. Phys.* **52**, 026502 (2013).
- <sup>20</sup>M. Wang and M. J. Kushner, *J. Appl. Phys.* **107**, 023309 (2010).
- <sup>21</sup>T. Shimmura, Y. Suzuki, S. Soda, S. Samukawa, M. Koyanagi, and K. Hane, *J. Vac. Sci. Technol. A* **22**, 433 (2004).
- <sup>22</sup>H. Ohtake, B. Jinnai, Y. Suzuki, S. Soda, T. Shimmura, and S. Samukawa, *J. Vac. Sci. Technol. A* **24**, 2172 (2006).
- <sup>23</sup>T. Ohmori and T. Makabe, *Appl. Surf. Sci.* **254**, 3696 (2008).
- <sup>24</sup>S. Rauf and A. Balakrishna, *J. Vac. Sci. Technol. A* **35**, 021308 (2017).
- <sup>25</sup>F. Gaboriau, G. Cartry, M.-C. Peignon, and C. Chardinaud, *J. Phys. D Appl. Phys.* **39**, 1830 (2006).
- <sup>26</sup>J. W. Coburn and H. F. Winters, *Appl. Phys. Lett.* **55**, 2730 (1989).
- <sup>27</sup>Y. Kim, S. Lee, T. Jung, B. Lee, N. Kwak, and S. Park, *Proc. SPIE* **9428**, 942806 (2015).
- <sup>28</sup>S. Samukawa and T. Mukai, *J. Vac. Sci. Technol. B* **18**, 166 (2000).
- <sup>29</sup>A. C. Westerheim, A. H. Labun, J. H. Dubash, J. C. Arnold, H. H. Sawin, and V. Y. Wang, *J. Vac. Sci. Technol. A* **13**, 853 (1995).
- <sup>30</sup>H. Ito, T. Kuwahara, K. Kawaguchi, Y. Higuchi, N. Ozawa, S. Samukawa, and M. Kubo, *J. Phys. Chem. C* **118**, 21580 (2014).
- <sup>31</sup>T. Kawase and S. Hamaguchi, *Thin Solid Films* **515**, 4883 (2007).
- <sup>32</sup>M. Wang, P. L. G. Ventzek, and A. Ranjan, *J. Vac. Sci. Technol. A* **35**, 031301 (2017).
- <sup>33</sup>D. Kim, E. A. Hudson, D. Cooperberg, E. Edelberg, and M. Srinivasan, *Thin Solid Films* **515**, 4874 (2007).
- <sup>34</sup>N. Kuboi, M. Fukasawa, and T. Tatsumi, *Jpn. J. Appl. Phys.* **55**, 07LA02 (2016).
- <sup>35</sup>M. Izawa, N. Negishi, K. Yokogawa, and Y. Momonoi, *Jpn. J. Appl. Phys.* **46**, 7870 (2007).
- <sup>36</sup>M. J. Kushner, *J. Phys. D Appl. Phys.* **42**, 194013 (2009).
- <sup>37</sup>Y. Zhang, M. J. Kushner, N. Moore, P. Pribyl, and W. Gekelman, *J. Vac. Sci. Technol. A* **31**, 061311 (2013).
- <sup>38</sup>A. Sankaran and M. J. Kushner, *J. Vac. Sci. Technol. A* **22**, 1242 (2004).
- <sup>39</sup>S. S. Kaler, Q. Lou, V. M. Donnelly, and D. J. Economou, *J. Phys. D Appl. Phys.* **50**, 234001 (2017).
- <sup>40</sup>N. A. Kubota, D. J. Economou, and S. J. Plimpton, *J. Appl. Phys.* **83**, 4055 (1998).
- <sup>41</sup>C. C. Cheng, K. V. Guinn, V. M. Donnelly, and I. P. Herman, *J. Vac. Sci. Technol. A* **12**, 2630 (1994).
- <sup>42</sup>C. F. Abrams and D. B. Graves, *J. Appl. Phys.* **86**, 2263 (1999).
- <sup>43</sup>J. M. Lane, K. H. A. Bogart, F. P. Klemens, and J. T. C. Lee, *J. Vac. Sci. Technol. A* **18**, 2067 (2000).
- <sup>44</sup>M. E. Barone and D. B. Graves, *Plasma Sources Sci. Technol.* **5**, 187 (1996).
- <sup>45</sup>A. Sankaran and M. J. Kushner, *J. Vac. Sci. Technol. A* **22**, 1260 (2004).
- <sup>46</sup>P. Traskelin, E. Salonen, K. Nordlund, A. V. Krashennikov, J. Keinonen, and C. H. Wu, *J. Appl. Phys.* **93**, 1826 (2003).
- <sup>47</sup>P. Traskelin, O. Saresoja, and K. Nordlund, *J. Nucl. Mater.* **375**, 270 (2008).
- <sup>48</sup>A. V. Vasenkov, X. Li, G. S. Oehrlein, and M. J. Kushner, *J. Vac. Sci. Technol. A* **22**, 511 (2004).
- <sup>49</sup>A. V. Vasenkov and M. J. Kushner, *J. Appl. Phys.* **95**, 834 (2004).
- <sup>50</sup>B. A. Helmer and D. B. Graves, *J. Vac. Sci. Technol. A* **16**, 3502 (1998).
- <sup>51</sup>S. B. Wainhaus, E. A. Gislason, and L. Hanley, *J. Am. Chem. Soc.* **119**, 4001 (1997).
- <sup>52</sup>J. C. Arnold and H. H. Sawin, *J. Appl. Phys.* **70**, 5314 (1991).
- <sup>53</sup>J. Matsui, K. Maeshige, and T. Makabe, *J. Phys. D Appl. Phys.* **34**, 2950 (2001).
- <sup>54</sup>B. M. Radjenovic, M. D. Radmilovic-Radjenovic, and Z. L. Petrovic, *IEEE Trans. Plasma Sci.* **36**, 874 (2008).
- <sup>55</sup>G. M. Sessler and J. E. West, *J. Appl. Phys.* **47**, 3480 (1976).
- <sup>56</sup>N. Marchack *et al.*, *J. Vac. Sci. Technol. A* **36**, 031801 (2018).
- <sup>57</sup>M. Schaepekens and G. S. Oehrlein, *J. Electrochem. Soc.* **148**, C211 (2001).